

ENGINE DESIGN AND OPERATIONAL IMPACTS ON PARTICULATE MATTER PRECURSOR EMISSIONS

Stephen P. Lukachko and Ian A. Waitz

Gas Turbine Laboratory
Department of Aeronautics and Astronautics
Massachusetts Institute of Technology
Cambridge, MA 02139

Richard C. Miake-Lye and Robert C. Brown

Center for Aerothermodynamics
Aerodyne Research, Inc.
Billerica, MA 01821

ABSTRACT

Aircraft emissions of trace sulfur and nitrogen oxides contribute to the generation of fine volatile particulate matter (PM). Resultant changes to ambient PM concentrations and radiative properties of the atmosphere may be important sources of aviation-related environmental impacts. This paper addresses engine design and operational impacts on aerosol precursor emissions of SO_x and NO_y species. Volatile PM formed from these species in the environment surrounding an aircraft is dependent on intra-engine oxidation processes occurring both within and downstream of the combustor. This study examines the complex response of trace chemistry to the temporal and spatial evolution of temperature and pressure along this entire intra-engine path, after combustion through the aft combustor, turbine, and exhaust nozzle. Low-order and higher fidelity tools are applied to model the interaction of chemical and fluid mechanical processes, identify important parameters, and assess uncertainties. The analysis suggests intra-engine processing is inefficient. For engine types in-service in the large commercial aviation fleet, mean conversion efficiency (ϵ) is estimated to be 2.8% to 6.5% for sulfate precursors and 0.3% to 5.7% for nitrate precursors at the engine exit plane. These ranges reflect technological differences within the fleet, the variation in oxidative activity with operating mode, and modeling uncertainty stemming from variance in rate parameters and initial conditions. Assuming sulfur-derived volatile PM is most likely, these results suggest emission indices of 0.06-0.13 g/kg-fuel assuming particles nucleated as $2\text{H}_2\text{SO}_4 \cdot \text{H}_2\text{O}$ for a fuel sulfur content of 500 ppm.

Keywords: particulate matter, sulfate, nitrate, emissions, inventory, environmental impact

1. INTRODUCTION

This paper addresses aircraft engine design and operational impacts on aerosol precursor emissions of oxidized sulfur and nitrogen species (*i.e.* $\text{SO}_x = \text{SO}_2 + \text{SO}_3 + \text{H}_2\text{SO}_4$, and $\text{NO}_y = \text{NO} + \text{NO}_2 + \text{HONO} + \text{HNO}_3$, respectively), focusing on sulfur trioxide (SO_3) due to its significant role in particulate matter (PM)

production relative to other emissions. Influential parameters and phenomena that control intra-engine oxidation are identified. Modeling techniques are outlined and uncertainties in predicted trace emissions evolution are assessed. Estimates for volatile particulate mass generated in the near-field exhaust of current, in-service commercial aircraft are presented as a function of operating mode. Our goal is to synthesize these investigations and present a first identification of technology trends in volatile PM emissions. This will enable inventory development for aviation PM and the assessment of associated air quality and climate effects. These results update and expand upon earlier work [1] with improved, validated modeling techniques and revised chemistry.

1.1. Aircraft particle emissions

Fine particles are emitted and generated in aircraft engine exhaust in size ranges constituting the nucleation, Aitken, and accumulation modes of a typical PM size distribution. Direct and indirect atmospheric effects from aviation-sourced PM constitute environmental risks of an uncertain magnitude [2,3].

Aviation-sourced PM emissions evolve over a large range of spatial and temporal scales. Aircraft directly emit non-volatile carbonaceous particles (soot) that are generated over millisecond time-scales within the combustor. *In situ* sampling of older in-service airframe-engine combinations suggests soot emissions at cruise are characterized by a lognormal distribution with a median diameter in the range of 20-60 nm, a geometric standard deviation on the order of 1.5-1.75, and a number emission index (EI) of $0.1\text{E}15$ - $6\text{E}15$ particles/kg-fuel [4-7]. Under current United States air quality rules, these particles would be defined as PM_{2.5} (particles smaller than a nominal 2.5 μm aerodynamic diameter). Assuming a soot density of 1500-1800 kg/m³, these data imprecisely place non-volatile EIPM (EIPM_{nv}) in the range of 0.002-2 g/kg-fuel, with a mean value of ~ 0.2 g/kg-fuel. The scaling of soot concentration with engine performance suggested in Döpelheuer [8] indicates this emission index range should also be representative of operational modes other than cruise.

Sulfate and nitrate production is initiated by gas phase oxidation of SO_2 and NO that begins in the post-combustion intra-engine flow. This gives a unique role to trace species chemical processing through the combustor dilution zone, turbine, and exhaust nozzle that is as important to the formation of volatile PM emissions as is the influence of combustor fluid mechanics on total NO_x ($\text{NO} + \text{NO}_2$), CO , and HC emissions. Our analysis addresses precursor emissions of trace nitrogen and sulfur oxides which are formed within the engine over time-scales on the order of 10 ms. These emissions contribute to the generation of volatile fine PM formed in the engine plume at longer time-scales (10 ms to < 1 s) compared to soot formation in the combustor.

As the exhaust plume mixes with the atmosphere, additional (secondary) PM may continue to form over days to weeks in air masses moving regionally hundreds of kilometers from the source. This is the result of further oxidation of emitted SO_x , NO_y , and HC species, typically via condensation or absorption onto existing particles. In this respect, soot continues to play a part in microphysical and chemical processes after emission. Over longer time-scales deposition occurs and additional aqueous and gaseous conversion processes can become important (*e.g.* reaction with ambient ammonia). This secondary processing has a different consequence than near-field plume and intra-engine oxidation, which are, to first-order, of greater importance to local perturbations in ambient PM concentration.

Volatile particles are smaller than non-volatiles but similarly described by a lognormal distribution, with median diameters in the range 1-15 nm, standard deviation on the order of 1.5, and number EIs 10-100 times greater than for soot. Using the modeling assessment described in this paper, we estimate the production of the aerosol precursors SO_3 and nitrous acid (HONO), as well as production of NO_2 , within the engine for in-service technology. Results are also presented for NO_2 , which is the source of another aerosol precursor nitric acid (HNO_3) that can be produced in the exhaust plume. Results are presented as a conversion efficiencies (ϵ), molar ratios defined as in Eq.(1).

$$\begin{aligned}\epsilon_{\text{SO}_3} &= \text{SO}_3/\text{SO}_x \\ \epsilon_{\text{HONO}} &= \text{HONO}/\text{NO}_y \\ \epsilon_{\text{NO}_2} &= \text{NO}_2/\text{NO}_y\end{aligned}\quad (1)$$

Based on SO_x precursors available at the engine exit, our analysis suggests that volatile EIPM (EIPM_v) can range from 0.06-0.13 g/kg-fuel assuming particles nucleated as $2\text{H}_2\text{SO}_4 \cdot \text{H}_2\text{O}$ for a fuel sulfur content of 500 ppm. These emissions indices are comparable to those for soot.

If all NO_y precursors available at the engine exit were also converted to PM, the EIPM_v may increase by a factor of 10-20. This is an unlikely event. One analysis of plume processing estimates emitted HONO uptake peaks at perhaps 10% for stratospheric temperatures, but the absorption is short-lived in the presence of SO_3 [9] and would undoubtedly peak at values lower than 10% in the troposphere where temperatures are higher. Our

estimates of EIPM_v do not include PM contributions sourced to HC species. Aircraft emit a range of gaseous hydrocarbons, which may also nucleate in the near-field region and add to the volatile PM mass [10,11]. Aircraft also emit engine oil, which contributes directly to volatile particulate mass by a currently unknown amount.

1.2. Outline

The discussion proceeds as follows. Section 2 describes the role of SO_x and NO_y emissions in aerosol formation, their consequent impacts on the atmosphere, and what is currently known about aircraft aerosol precursor emissions. We then model the interaction of chemical and fluid mechanical processes using both low-order and higher fidelity tools. Our approach is to build an understanding of the key parameters and uncertainties in trace emissions prediction in order to establish a firmer connection between technology and environmental impact.

Section 3 discusses the methods used to determine physical drivers and to develop estimates for trace species emissions, and details the parameter space investigated. Sections 4 and 5 focus on cycle-level effects, employing a low-order, comparative time-scale methodology and 1-D models over averaged flow properties through the combustor, turbine, and exhaust nozzle to investigate fundamental trends in SO_x and NO_y oxidation as a function of engine technology and flight condition.

Section 6 addresses two areas of uncertainty in these results. Section 6.1 looks at error in the specification of initial conditions and reaction parameters. Further investigation with higher fidelity, unsteady 2-D computational tools presented in Section 6.2 focuses on the role of temperature and velocity non-uniformities associated with turbine fluid mechanical phenomena in determining trace species chemistry. This provides a quantification of uncertainties related to methodological choice in modeling intra-engine processing. Section 7 synthesizes the analyses of Sections 3-6 and presents estimates for EIPM_v .

2. AIRCRAFT VOLATILE PM EMISSIONS

Various mechanisms lead to the production of particulate precursors within the engine. Oxidized nitrogen species originate primarily from the high temperature oxidation of atmospheric nitrogen in the combustor. Total sulfur emissions are predictable functions of fuel composition and emerge from the primary zone as SO_2 in lean conditions. Sulfur emissions are thus controlled by fuel consumption to a greater extent than NO_x . Formation of precursors to volatile PM, including SO_3 and HONO, initiates within the combustor and continues downstream through the turbine and exhaust nozzle [1,12-14]. The response of trace chemistry to the temporal and spatial evolution of temperature and pressure through the turbine is complex and presents both computational and experimental challenges. Total emissions are related to the technological characteristics of the aircraft (weight, aerodynamic efficiency, and engine overall efficiency), its operational use, and details of the combustor, turbine, and nozzle design.

2.1. Precursors, microphysics, and effects

Experimental and modeling studies have highlighted the role of trace emissions of SO_3 in the formation of high number densities of fine aerosol particles observed in the exhaust streams of several aircraft [5-7,11,15-17]. Particle concentrations are correlated with the level of oxidized fuel sulfur in the exhaust [6,18]. At exhaust temperatures and lower temperatures, SO_3 converts to H_2SO_4 in the presence of exhaust water vapor [19]. In the plume, new volatile sulfate particles can be formed by binary homogeneous nucleation of H_2SO_4 with emitted water vapor [20], accentuated by concomitant chemiion emissions [21]. Nucleated sulfate particles grow via coagulation and uptake of water vapor [22,23]. Because nitrous and nitric acids have high saturation vapor pressures relative to sulfuric acid, they have a lesser tendency to nucleate new particles and thus contribute to PM primarily via uptake on existing particles. Hydrocarbons can also contribute via uptake, and may additionally nucleate as an independent PM source [24], but thermodynamic conditions are not favorable for this process at the HC levels typically emitted [25]. Both HNO_3 and H_2SO_4 are emitted in concentrations orders of magnitude smaller than SO_3 and HONO, thus evaluation of volatile aviation PM should focus on the latter species. The results of our analysis point out that production of H_2SO_4 from emitted SO_3 is greater in magnitude than new sulfuric acid production in the plume. Although production of HNO_3 occurs at rates about an order of magnitude lower than for H_2SO_4 at exhaust and ambient conditions [26], HNO_3 can play a role in plume PM processing [27]. We thus also examine intra-engine production of NO_2 , the chemical precursor to nitric acid. Note that condensed matter can further increase through heterogeneous nucleation of sulfuric acid on soot and metal surfaces, activated by adsorption of oxidized sulfur, in the presence of water vapor [16]. This analysis does not address such interactions between non-volatile PM and aerosol precursors.

Particles formed can perturb the mass and size distribution of the background atmospheric aerosol if scavenged, alter the chemical makeup of the upper atmosphere through heterogeneous chemistry, and perhaps freeze, persisting as contrail particles. Microphysical processes involving emitted and generated particles can lead to changes in contrail optical properties, but have minimal apparent impact on formation tendency [11]. However, the incidence of persistent contrails is expected to increase as aircraft engines become more efficient [28]. Measurements suggest the presence of radiative impacts from aviation contrails and related cirrus [29], but the effect of aerosols on clouds is not well understood [30]. Particles may play a part in cirrus formation near flight tracks, via contrail evolution into cirrus for example, and as a result of the greater spatial coverage that results, aviation-induced cirrus impacts are expected to be larger than contrail impacts [31-33]. Comparatively, direct sulfate radiative forcing has been estimated as a relatively small, negative impact [3]. Although there is high uncertainty, the collective instantaneous radiative impact of contrails and clouds is estimated to be greater than

that of aviation CO_2 and NO_x emissions combined. Accounting for all aviation perturbations, models suggest the present day aviation particulate-related contribution to total anthropogenic forcing from aircraft is greater than 2% [3,34]. This contribution is expected to increase with air transportation growth.

The role of aviation PM in determining local air quality is poorly understood, partially due to incomplete characterization of particulate emissions from in-service aircraft. Fine PM is associated with the incidence of mortality and illness, including both acute and chronic respiratory and cardiac health endpoints, and can lead to visibility impairment. Upon deposition, PM contributes to ecosystem damage resulting from acidification as well as soiling and other materials damages [2].

2.2. Measurement and modeling

Experimental data characterizing sulfur species in engine exhaust consist primarily of concentrations inferred from in-flight plume measurements [6,7,11] and a few direct measurements at and downstream of the engine exit plane [35-37], mostly at higher power conditions for older in-service commercial and military aircraft. Inferred levels indicate an apparently broad range of SO_2 to H_2SO_4 oxidation. However, a detailed analysis of the instrument responses and age of the sampled air has refined the estimates of oxidative conversion to 0.5-5% of the fuel sulfur [38]. In-flight trends and ground measurements suggest oxidation efficiency is dependent on engine technology and operating point [11,37]. For comparison, measurement of land-based, marine, and laboratory test gas turbines burning diesel fuel demonstrate oxidation to SO_3 of between 2 and 22% [39].

Measurements of NO and NO_2 are routine in engine development and certification, but there are few measurements of their oxidation products, HONO and HNO_3 . These species have been predicted to be present in aircraft exhaust [1,13], and measurements of HNO_3 and HONO [40,41] have indicated that conversion of NO to HONO and NO_2 to HNO_3 at the engine exit plane amounts to a few percent or less at higher power conditions. Intra-engine conversion of NO to NO_2 has been estimated from measurements at much higher levels, up to ~25% [42].

Because nucleation rates are high for H_2SO_4 given typical fuel sulfur levels, modeling investigations of the microphysical processes that lead to the formation of volatile aerosols emphasize the development of oxidized sulfur through the aircraft plume and wake. These investigations find that known gaseous pathways yield only 1-2% oxidation within the near-field plume (< 1 s after emission) for a range of aircraft engine configurations, physical approximations, and chemical assumptions [22,43]. Modeling investigations have also shown that compared to the plume, sulfur oxidation can be more vigorous within the aircraft engine as a result of gaseous chemical processes through the combustor dilution zone, turbine, and exhaust nozzle. Upper bound chemical kinetic analyses indicate that SO_3 formation via atomic oxygen is less than 6% of SO_x within the combustors used in aircraft [12] and industrial applications [44]. Previous studies have also suggested SO_3 formation via OH and O may

result in an upper limit 10% oxidation through the turbine and nozzle [1,12-14,45].

Accounting for key factors influencing post-combustion intra-engine processing, revised trace chemistry, and the thermodynamic behavior of in-service aircraft types under typical operational conditions, this study finds intra-engine conversion efficiencies of SO₂ to SO₃ for commercial aircraft are within this upper bound limit. Our modeling analyses presented here are also consistent with reported experimental results.

3. METHODS

Our analysis uses a simulation methodology for aerosol precursor behavior that has been previously introduced. Reacting flow simulations are exercised with fidelity appropriate to the magnitude of flow non-uniformity, particularly in temperature, along the gas path. This study finds that low-order models of the active chemistry, where kinetics are driven by averaged flow parameters specified as a function of time, capture the impact of fluid properties on trace NO_y chemistry within the engine. Non-uniformities can, however, have a significant influence on trace SO_x chemistry. In order to estimate the magnitude of the effect on sulfate precursor emissions, a more complex fluid dynamical representation is constructed. These higher fidelity computations need only be applied to regions of the engine flow path that, because of thermodynamic conditions and favorable residence time, exhibit trace species activity which could be influenced by non-uniformity of the intra-engine flow. We use comparative time-scale analyses such as those discussed in Section 4 to identify regions along the gas path that fit this description, and observe that it is usually not necessary to increase fidelity for engine sections downstream of the high-pressure turbine (HPT). For this analysis, a 2-D, unsteady computation for the first stage of the high-pressure turbine is developed to evaluate multi-dimensional effects. Lower fidelity, 1-D simulations suffice as the alternative for the remaining sections of the gas path.

Additional methodological details are described in the following sections. In Whitefield *et al.* [41], estimates for emissions levels using this approach correctly captured trends and matched experimental data within measurement uncertainty for the conversion of NO to HONO at both the combustor and nozzle exits of a test engine. This provided support that OH-driven oxidation of NO_x can be modeled with acceptable accuracy. Similar OH-driven kinetics also control the oxidation of SO₂ to SO₃, for which direct measurements are not available. However, favorable results for estimating HONO and the availability of appropriate SO_x kinetic parameters suggests that the modeling of SO_x oxidation should also provide good estimates of the exit sulfur emissions speciation. Section 4 further explores the foundations and applications for the methodology described, using a comparison of physical and chemical time-scales to establish the relative importance of various controls on oxidation, and relating such influences to aircraft engine design parameters.

Table 1. Cycle parameter specification for time-scale and flow-averaged 1-D gas path simulations

EINO_x as NO₂ and EIS = 0.5 g/kg-fuel. EICO and OFAR different for each cycle and condition. Common initial species conditions are: (a) NO/NO_x = 1; (b) SO/SO_x = 0; (c) no HC or H₂. Note combustion efficiency is consistent with EICO.

Class (kN)	<100		100-200		200-400		>400	
Thrust (kN)	60	65	100	170	205	230	250	420
Case #	1	2	3	4	5	6	7	8
Take-off								
P ₃ (atm)	16	15	23	25	20	27	27	37
T ₄ (K)	1350	1200	1520	1510	1400	1560	1540	1940
EINO _x (g/kg-fuel)	35	19	55	17	36	30	27	20
Climb								
P ₃ (atm)	14	12	19	22	17	24	23	31
T ₄ (K)	1300	1140	1440	1450	1340	1510	1480	1840
EINO _x (g/kg-fuel)	29	16	42	14	27	24	22	16
Cruise								
P ₃ (atm)	6.0	5.7	8.0	9.0	7.1	7.3	9.7	13
T ₄ (K)	1170	1030	1340	1340	1270	1210	1370	1710
EINO _x (g/kg-fuel)	5.1	7.1	7.1	6.3	8.2	7.6	9.4	5.9
Approach								
P ₃ (atm)	6.0	5.7	7.1	9.2	7.6	10	9.8	13
T ₄ (K)	960	870	1010	1080	1010	1140	1110	1440
EINO _x (g/kg-fuel)	9.3	8.4	10	6.0	7.3	10	11	5.5
Idle								
P ₃ (atm)	2.6	2.6	3.3	3.7	3.3	4.4	4.0	5.3
T ₄ (K)	750	710	840	870	830	940	900	1220
EINO _x (g/kg-fuel)	3.7	8.4	6.0	4.0	2.9	4.2	4.7	2.4

Table 2. Parameter specification for 2-D unsteady turbine stage simulations

Common initial species conditions are:
 (a) NO/NO_x = 1; (b) SO/SO_x = 0; (c) no HC or H₂.
 EINO_x = 15 g/kg-fuel and EIS = 0.5 g/kg-fuel for all cases.
 Note combustion efficiency is consistent with EICO.

Parameter specifications	FSC (ppm)	Pattern factor	Range T ₄ (K)
Higher power cases			
T ₄ = 1900 K; P ₃ = 22 atm; T _{surf} = 850 K (NGV), 775 K (rotor)			
Case 1	500	30%	1550-2250
Case 2	500	10%	1800-2000
Case 3	10	30%	1550-2250
Case 4	10	10%	1800-2000
Lower power cases			
T ₄ = 1300 K; P ₃ = 7 atm; T _{surf} = 640 K (NGV), 590 K (rotor)			
Case 5	500	30%	1100-1500
Case 6	10	30%	1100-1500

3.1. Parameter specification

Initial species and flow conditions for the time-scale, flow-averaged 1-D, and higher resolution 2-D unsteady computations were specified to highlight technological and operational trends in particulate emissions from the current

commercial aviation fleet. A number of engine thermodynamic cycles were developed to represent the range of engine types in service on large commercial aircraft. Temperature and pressure profiles as a function of time were specified for each of five operating modes: the four certification settings, idle/taxi, approach, climb, and take-off, and a fifth setting to represent the altitude cruise condition. These were used directly as the flow parameter specification for the time-scale and 1-D simulations discussed in Sections 4 and 5. Table 1 summarizes these cycles by thrust class.

The 2-D analyses reviewed in Section 6.2 for a representative single turbine stage were specified at flow conditions also spanning the parameter range of large commercial engines in service. Simulation parameters were varied to highlight fluid mechanical impacts on oxidation through the post-combustor flow path, for a range of fuel sulfur levels, power conditions, and pattern factors. Table 2 summarizes the conditions examined.

3.2. Chemistry and initial conditions

A prerequisite for the simulation capability is the availability of finite rate kinetic mechanisms that apply to conditions intermediate between combustion and atmospheric chemistry. The full mechanism used for the computations described here was truncated from the larger set developed in Mueller *et al.* [46] based on previous studies and new laboratory experiments [see also 47]. A reaction list can be found in the Appendix.

For computations addressing chemistry aft of the combustor, initial trace species concentrations are determined at the turbine inlet using the pressure, temperature, and overall fuel-air ratio (OFAR) relevant to the conditions specified in Table 1 and Table 2; combustor SO_x or NO_y oxidation is initialized using a similar methodology, but at a stoichiometric FAR. To best identify technology trends given the complexity of the combustor flow-chemistry environment, we chose to parameterize trace chemical activity in the combustor dilution zone in Section 5.1 using a separate set of computations to provide a full account of aerosol precursor levels at the engine exit. It is possible to simply add these results to the oxidation estimated to occur from the turbine inlet to nozzle exit [12,13]; sensitivity parameters discussed in Section 6.1 suggest that the low levels of SO₃ and HONO formed in the combustor have a minor effect on subsequent oxidation, translating instead into equivalent conversion at the engine exit.

Estimation of species initial conditions at the turbine inlet starts with equilibrium concentrations at the given flow conditions and FAR. Concentrations for species known not to be in equilibrium (*e.g.* NO_x, SO_x, and CO) are then changed to levels measured during certification tests of the engines on which the representative cycles are based while maintaining elemental balance. This calibration of emission indices is followed by a short constant temperature and pressure kinetic calculation adjustment to allow the species to achieve quasi-steady state. This final step removes any non-physical, rapid readjustments of concentrations in the mixture that result from the imposed changes to the mixture. These rapid readjustments

occur for reactive species that are sensitive to the distribution of NO_x, SO_x, and CO and have relatively short characteristic time-scales. Although oxidation within the SO_x and NO_y families may be significant, species family total EIs are basically invariant through the engine. Fuel sulfur levels are set at a constant 0.5 g/kg-fuel (500 ppm) for all 1-D analyses, but vary as specified in Table 2 for the 2-D simulations (10-500 ppm). All other species initial conditions, including OH, O, HO₂, and H are set to their equilibrium values at the specified temperature and pressure. The initial ratios of NO/NO_x and SO₂/SO_x are set to 1.0.

4. DETERMINANTS OF INTRA-ENGINE OXIDATION

The evolution of aerosol precursors is controlled by the thermodynamic potential for formation (referenced to equilibrium, and changing with T and P), chemical kinetic rates, and the flow residence time available to complete reactions. Engine cycle, internal turbomachinery fluid mechanics, and engine size determine temperature, pressure, and residence time. For trace species interactions through the combustor dilution zone, turbine, and exhaust nozzle, heat release is negligible except in conditions where the combustor is operated at fuel-air ratios higher than those employed in current commercial aircraft engines. Since oxidation activity generally decreases with lower temperatures and pressures, power extraction in the turbine acts as a limit on the extent of intra-engine oxidation. Such constraints are not fully countered by the increase in thermodynamic potential, as equilibrium levels of oxidation products increase with lower temperatures. There are also

Table 3. Reduced reaction sets describing SO₃, HONO, and NO₂ kinetics

Reaction* troe = Troe form parameters low = low pressure parameters	A units: cm-mol-sec-K E units = cal / mol		
	A	b	E _a
SO₃			
1 SO ₂ + O (+M) → SO ₃ (+M) † troe: n/a low →	9.20E+10 4.00E+28	0.00 -4.00	2.384E+03 5.250E+03
2 SO ₂ + O → SO ₂ + O ₂	0.44E+12	0.00	0.610E+04
3 SO ₂ + OH = SO ₃ + H	0.49E+02	2.69	0.238E+05
4 SO ₂ + OH (+M) = HOSO ₂ (+M) † troe: 0.35 / 1e-30 / 1e30 low →	1.21E+12 1.87E+31	0.00 -4.61	0.000E+00 2.050E+03
5 HOSO ₂ + O ₂ = SO ₃ + HO ₂	7.80E+11	0.00	0.656E+03
NO₂			
6 NO + O (+M) → NO ₂ (+M) troe: 0.957 / 1e-90 / 1551e03 low →	1.30E+15 4.72E+24	-0.75 -2.87	0.000E+00 1.551E+03
7 NO ₂ + O → NO + O ₂	1.05E+14	-0.52	0.000E+00
8 NO ₂ + H → NO + OH	1.32E+14	0.00	3.620E+02
9 NO + HO ₂ = NO ₂ + OH	2.11E+12	0.00	-4.790E+02
HONO			
10 HONO + OH → NO ₂ + H ₂ O	1.70E+12	0.00	-5.200E+02
11 NO + OH (+M) = HONO (+M) troe: 0.62 / 1e-90 / 1e+90 low →	1.99E+12 5.08E+23	-0.05 -2.51	-7.210E+02 -6.760E+01
12 HONO + O = OH + NO ₂	1.20E+13	0.00	5.961E+03

Notes:

* Irreversibility (→) in a reaction was considered only when differences between forward and backward rates differed by more than 3 orders of magnitude. For reactions 4 and 6, Troe form used here is different from original references.

† Efficiencies for R1: N₂ = 1.3, H₂O = 10; for R4: H₂O = 10.

kinetic limits on oxidation, such as the availability of O, OH, and HO₂, which evolve primarily through self-reactions [13,46,47]. These species, along with NO_x, SO_x, CO, and HC, are found at the turbine inlet in concentrations established by combustion and dilution processes in the combustor. With temperature and pressure, they determine reactivity. Within the engine, heterogeneous oxidation pathways are of minimal consequence to aerosol precursor production [48]. Thus, gaseous chemistry is our focus.

4.1. Kinetic influences

In Table 3, reduced sets of reactions specific SO₃, HONO, and NO₂ formation are listed that highlight the primary kinetic influences on post-combustion oxidation.

Reactions were selected from the reaction mechanism listed in the Appendix based on ranked contribution to production rates for the species of interest over the post-combustion flow path for the range of engine cycle parameters listed in Table 1. While the reduced reaction sets listed in Table 3 preserve the relevant formation dynamics, their use in a predictive manner can result in deviations of up to 25%. In addition to the nitrous acid production outlined, production of sulfuric and nitric acids depends on formation of SO₃ (SO₃ + H₂O → H₂SO₄) and NO₂ (NO₂ + OH → HNO₃) described by these kinetics.

There are two pathways leading to SO₃ formation represented in Table 3, via OH and less importantly via O, mediated to a minor extent by consumption via H. For SO₃, reactions 1 and 2 (R1 and R2) constitute a partial recombination of atomic oxygen to form molecular oxygen, O + O = O₂. However, the rate of destruction of SO₃ by R2 is typically much less than the rate of production by R1. R3 is a reductive reaction, but the limited availability of atomic hydrogen limits the strength of this destruction pathway to approximately ten times less than R2. R4 and R5 represent formation of SO₃ via an OH pathway, which dominates SO₃ dynamics in the regime intermediate between atmospheric conditions and combustor conditions.

Similar to SO_x chemistry, O and OH are central to NO_y chemistry. Although NO₂ and HONO are necessarily coupled in the full mechanism shown in the Appendix they are isolated here to highlight the relevant kinetics. Like SO₃, R6 and R7, which contribute to NO₂ kinetics, represent O + O = O₂, but compared to the corresponding dynamic in the sulfur chemistry, the resultant impact on NO₂ can be either positive or negative. However, formation of NO₂ is typically dominated by R9 via HO₂ as opposed to the O pathway. Destruction by H has a larger role than for SO₃, but is still relatively minor. Reaction R11 involving OH primarily determines formation of HONO.

Characteristic time-scales for SO₃, HONO, and NO₂ formation can be derived from the sets of reactions listed in Table 3 as shown in Eq.(2). Terms in Eq.(2) depend on specification of H, O, OH, HO₂, and O₂ concentrations, as well as reservoir species such as N₂ and H₂O to account for efficiencies. The coefficients C_x depend primarily on temperature. For Eq.(2), HOSO₂ in R5 is determined by a pseudo steady-state equilibrium

using R4 and R5 in a relative abundance of O₂. Eq.(2) also assumes NO_x and SO_x concentrations remain constant.

At equilibrium for typical turbine conditions, the molar ratios of O/OH and HO₂/OH are of order 0.01, and H/OH is of order 0.00001. To illustrate the relative contributions of OH, HO₂, O, and H to oxidation reactivity in the turbine, relative trends for the terms in Eq.(2) using these approximate equilibrium molar ratios are shown in Figure 1 for a range of temperatures. In Figure 1, the larger the relative value, the faster the chemistry and the greater the contribution. At any given temperature, pathways involving HO_x are generally most consequential to trace chemical reactivity; atomic oxygen has a role, but for the equilibrium ratios relevant to these cycles, it is a minor contributor, requiring an increase in concentration by a factor of 100 to be of comparable importance along the gas path.

$$\tau_x [\text{OH}] = \left\{ C_{\text{OH}} + C_{\text{const}} \frac{1}{[\text{OH}]} + C_{\text{O}} \frac{[\text{O}]}{[\text{OH}]} + C_{\text{HO}_2} \frac{[\text{HO}_2]}{[\text{OH}]} + C_{\text{H}} \frac{[\text{H}]}{[\text{OH}]} \right\}^{-1}$$

	SO ₃	HONO	NO ₂	
C _{OH}	$k_4 \left(\frac{k_5 [\text{O}_2]}{k_{4b} + k_5 [\text{O}_2]} \right)$	$k_1 + k_{3b}$	k_{4b}	
C _{const}	0	k_{2b}	0	(2)
C _O	$k_1 + k_2$	k_3	$k_1 + k_2$	
C _{HO₂}	$k_{5b} \left(\frac{k_{4b}}{k_{4b} + k_5 [\text{O}_2]} \right)$	0	k_4	
C _H	k_{3b}	0	k_3	

O_x and HO_x equilibrate within the engine on time-scales faster than consumption by trace families, and as a result, the relative consumption of reactive oxidation species associated with the SO_x and NO_y chemistries, for a given rate of temperature change, is of primary consequence to conversion efficiencies (ε). The blue shaded areas in Figure 1 show the typical range of temperatures and characteristic chemical time-scales found in the thermodynamic environments of the HPT and LPT. Specific examples of time-scale trends as a function of temperature for constant pressures characteristic of the LPT and HPT, 1 atm and 10 atm respectively, are shown with dashed lines. In general, despite large equilibrium values for SO₃, HONO, and NO₂ at the flow conditions of the engine exit, oxidation time-scales are too long to allow significant conversion along the engine gas path. For common, in-service engines, the characteristic time-scale for SO₃ is approximately 100 ms, increasing to values greater than 1 s at the nozzle exit. Comparatively, the flow-through times for the post-combustor flow path are much shorter, typically between 1-10 ms.

Conditions in reference to Eq.(2): $O/OH = 1E-2$, $HO_2/OH = 1E-2$, $H/OH = 1E-5$
 Characteristic chemical time-scale τ_c : HPT at P = 10 atm, LPT at P = 1 atm

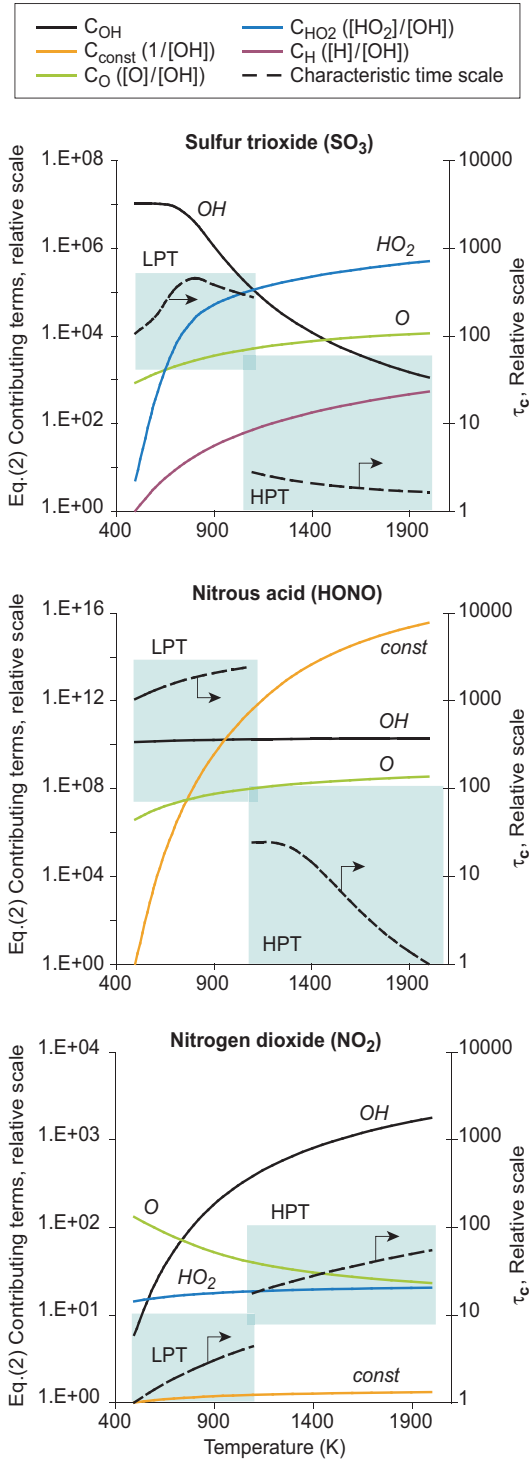


Figure 1. Chemical kinetic drivers of trace SO₃, HONO, and NO₂ chemistry.

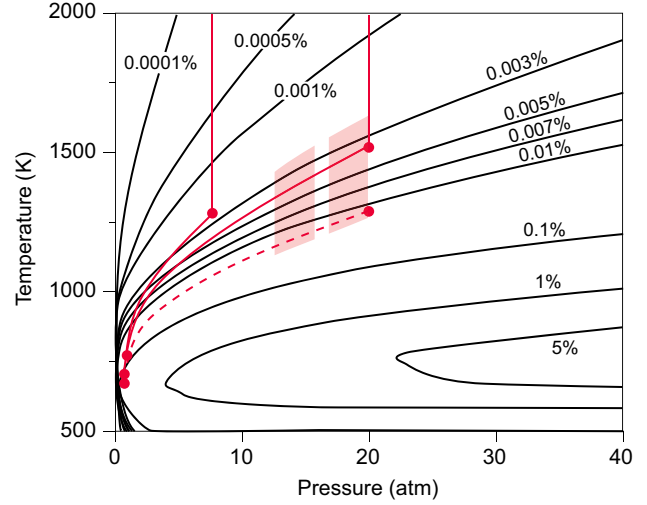


Figure 2. Conversion potential ($\Delta\epsilon_{SO_3}$) as a function of temperature and pressure. To calculate ϵ' , the fuel hydrogen-carbon ratio (H/C) is set at 2, and the FSC is specified at 500 ppm, both representative of Jet A fuel.

4.2. Conversion potential

To exemplify the trade between thermodynamic potential and kinetic time-scale as a function of temperature and pressure, a comparison of fluid and chemical time-scales for SO₃ production is constructed in Eq.(3), defining a conversion potential, $\Delta\epsilon = \Delta SO_3/SO_x$. The definition assumes that $[SO_3] \gg [H_2SO_4]$, which is true for all but a few parameter ranges as discussed in Section 5. Fluid mechanical and chemical kinetic influences are represented through a Damköhler (Da) number, and thermodynamic potential is defined as the equilibrium conversion efficiency (ϵ').

Equilibrium SO_x depends on temperature and pressure, shifting toward SO₃ at low temperatures, and is only weakly dependent on pressure, increasing from <10% at the combustor exit to ~90% at the nozzle exit. Increasing fuel sulfur level generally decreases the resulting ratios at equilibrium, but as will be evident in later sections, fuel sulfur level has minimal consequence for oxidation levels. As defined, $Da > 1$ indicates that 95% of ϵ' is reached within the reference flow residence time, and $Da < 1$ indicates that only a fractional conversion is attained.

$$\Delta\epsilon = \begin{cases} Da[\epsilon' - \epsilon] & \text{for } Da_{SO_3} \leq 1 \\ \epsilon' & \text{for } Da_{SO_3} > 1 \end{cases} \quad (3)$$

$$Da = \frac{\tau_{flow}}{\tau_{SO_3}}$$

$\epsilon' = \epsilon$ at equilibrium

Figure 2 maps $\Delta\epsilon$ for a small increment in flow time of ~0.1 ms (a flow-through time for a single blade row) and an initial converted fraction of 0%. Iso- $\Delta\epsilon$ contours indicate oxidation potential >1% over this time-scale only for a range of temperatures between 600 K and 900 K and pressures over

~5 atm. Conditions of this description are experienced by limited portions of the core flow, specifically in the combustor dilution zone flow at low power, and areas interacting with cooling flows, at locations typically within the combustor or high-pressure turbine. The bulk flow evolution through the turbine and beyond is generally outside this region for all engine operating modes.

The strength and location of regions of high oxidation potential would necessarily evolve as S(VI) is formed (ϵ increases as the gas path is traversed). Moving from the upper right of Figure 2 to its lower left traces a generalized path of oxidation potential that follows the change of temperature and pressure from turbine inlet to nozzle exit. Two example thermodynamic paths are shown, one representative of the take-off condition and one for cruise. Also shown on Figure 2 is the path of constant pressure processing through the combustor dilution zone. We will consider this further in Section 5.1. The shaded areas represent the influence of spanwise temperature non-uniformities in the turbine as discussed in Section 6.2.

The form of the contours in Figure 2 is representative of results for NO_2 and HONO as well, with the exception that peak conversion potential occurs at lower temperatures for NO_2 , and even lower for HONO. In addition, the contours tend to be more spread for NO_2 and less so for HONO relative to SO_3 , a consequence of the relative range of chemical time-scales over the gas path (see Figure 1). As a result, HONO oxidation tends to exhibit a greater dependence on power setting than with SO_x . HONO production is typically limited to a smaller axial section of the flow path at lower temperatures than SO_3 or NO_2 . By this account, HONO production should also exhibit a greater sensitivity to temperature than SO_3 . However, cross-stream temperature non-uniformities, which play a relatively important role in SO_3 production, are less significant in the lower pressure flow path where HONO is formed.

5. TECHNOLOGICAL AND OPERATIONAL TRENDS

In this section, estimates of post-combustion SO_3 , HONO, and NO_2 production through the combustor dilution zone, turbine, and exhaust nozzle are obtained using 1-D chemical kinetic calculations through averaged gas path temperature and pressure profiles derived from the 8 cycles described in Table 1. Section 5.1 develops a parameterization of trace chemical activity in the combustor dilution zone. The objective is to place bounds on the likely conversion efficiency at the turbine inlet for a range of combustor designs operating in the current fleet. Section 5.2 then addresses trace chemistry through the expansion gas path. Together, these analyses enable identification of technological and operational trends. Uncertainties in these results are discussed in the following Section 6, which evaluates the robustness of the result to changes in rate parameters and initial conditions and the impact of introducing more realistic fluid mechanics.

5.1. Combustor oxidation

Two parameters were independently varied to examine the range of potential oxidation levels at the combustor exit—

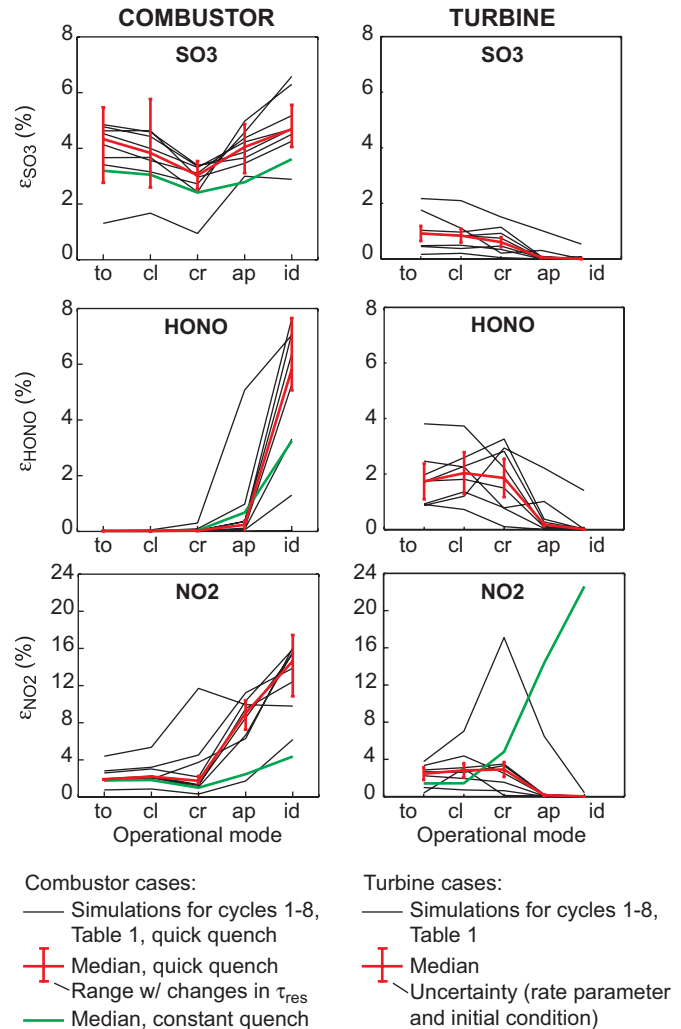


Figure 3. Intra-engine conversion efficiencies (ϵ_{SO_3} , ϵ_{HONO} , and ϵ_{NO_2}) estimated using 1-D flow-averaged simulations.

residence time (τ_{res}) and rate of dilution air addition. In one case, referred to here as the *quick quench* case, all dilution air is added over a period of 1 ms to reach the turbine inlet temperature, and then trace chemistry is allowed to continue for additional residence times of 1-15 ms. In the other case, dilution air is added at a constant rate for a total residence time, τ_{res} , of 2-16 ms (the *constant quench* case). This parameter space represents upper and lower bounds on the technologies associated with the engine types simulated, but the quick quench case is more likely representative of in-service combustor design. Note that as cycle T_4 increases, the amount of combustor dilution air added necessarily decreases and the response to dilution schedule becomes less important.

For the analysis, the upstream boundary is defined by the location of peak combustion temperature at a stoichiometric fuel-air ratio (FAR). The physical location of this point may vary among combustor designs, but it uniformly defines when

an oxidative environment would be achieved, and this is a necessary precondition to precursor production. Other than the specification of the initial stoichiometric FAR, the methodology described previously in Section 4 to establish species conditions is employed, using the same values for E_{NO_x} and EIS listed in Table 1. For each case, combustor conversion efficiency was explored using a 1-D model (averaged, fully-mixed conditions) varying temperature profiles at constant pressure. The temperature profiles are specified by the different dilution schedules, enforcing different rates of temperature change from a flame temperature estimated using T_3 calculated for the cycle, to T_4 as listed in Table 1.

The results of this simplified representation of the combustor suggest attention must be paid to dilution zone processing, which is likely the primary location for sulfate aerosol precursor production over all modes, and at low power conditions for nitrate precursors. Figure 3 shows results for conversion efficiency for the quick quench case where τ_{res} is 6 ms. Median combustor ϵ_{SO_3} is highlighted in red. For comparison, median ϵ_{SO_3} is shown in green for the constant quench case. These medians span a range of 2.5-4.5% over the five operating modes.

The dependence on cycle temperatures and pressures is not monotonic. A clearer picture of trends in SO_3 production in the combustor can be described with reference to the vertical profile section of thermodynamic paths drawn on Figure 2 representing the dilution zone flow. These constant pressure profiles fall within higher contours of conversion potential as T_4 is reduced, however lower operating temperatures are correlated with lower operating pressures, which follows the contours of $\Delta\epsilon$. The influence of pressure, and by implication altitude, is evident in Figure 3 comparing ϵ_{SO_3} for the cruise condition to the 4 LTO modes. The range shown by the red whiskers in Figure 3 shows the variation of median ϵ_{SO_3} with τ_{res} . Higher ϵ_{SO_3} is correlated with higher τ_{res} , but the range is narrower than the variance sourced to rate parameter and initial condition uncertainty discussed in Section 6.1. The higher the τ_{res} in the combustor, the more likely it is that equilibrium ϵ_{SO_3} will be found at the turbine inlet.

Combustor ϵ_{SO_3} is higher than the estimates for median ϵ_{SO_3} through the rest of the gas path. The combustor plays a more limited role in the production of HONO and NO_2 where dilution zone processing is dominant only for lower power conditions. For NO_y , the impact of residence time is not monotonic, suggesting the more complex kinetic response to the thermodynamic environment seen for oxidation through the turbine and exhaust nozzle. A significant combustor role in determining ϵ_{HONO} in comparison to downstream engine sections is observed only at the idle condition (6% median at idle versus <0.1% at other conditions). Median ϵ_{NO_2} at take-off, climb, and cruise is comparable to subsequent oxidation, but similar to HONO, there is a much stronger combustor oxidation contribution at lower power conditions (median 8% at approach and 14% at idle).

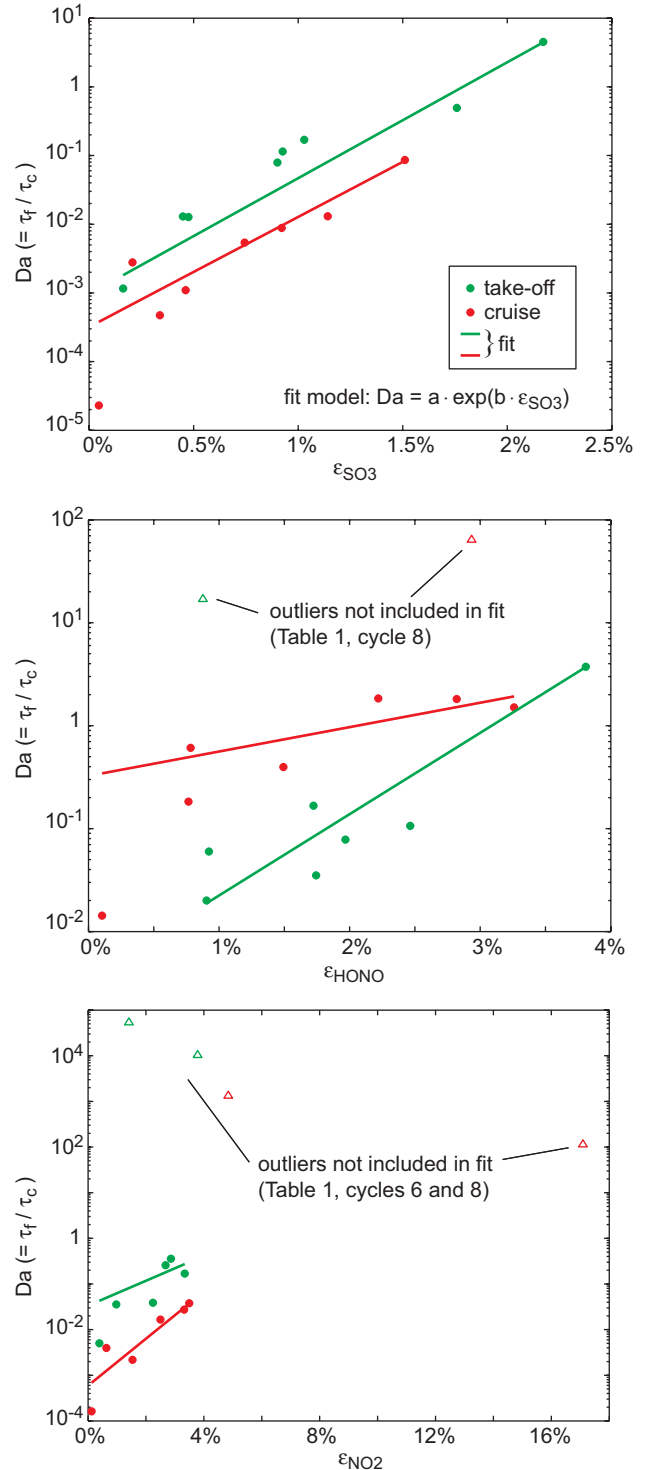


Figure 4. Explanation of variance in conversion efficiency trends as a function of technology and flight condition using Da.

5.2. Turbine and exhaust nozzle oxidation

The impact of cycle design on ϵ through the turbine and exhaust nozzle is reflected primarily through the influence of peak temperature, and to a lesser extent, peak pressure. As cycles become hotter and reach higher overall pressure ratios, post-combustor trace chemical activity will tend to increase. The use of cooling air has also increased as a necessary enabler for hotter cycles, with more blade rows in the HPT and LPT subject to some protection to achieve life requirements. This further increases the opportunity for oxidation as described later in Section 6.2. However, importantly, turbine design choices set the time rate of change of temperatures and pressure along the gas path. This rate is a function of blade loading, which has increased since the introduction of the jet engine, tending to reduce the opportunity for large conversion; the number of stages is reduced and residence time at any one temperature and pressure decreases. For similar size engines shown in Table 1, intra-engine residence time has generally decreased historically (but increases with engine size / thrust class).

Figure 3 summarizes technology and operational trends in aerosol precursor production along the turbine and exhaust nozzle gas path. Figure 3 shows the range of ϵ over all cycles as a function of operating mode. The red line indicates the median trend with propagated uncertainties, discussed further in Section 6.1, denoted by the whiskers. While thermodynamic conditions would support high conversion efficiencies, the results show the strong kinetic limitations of the turbine environment on aerosol precursor production. In Figure 3, conversion efficiencies generally increase with power level, or more generally with higher peak temperature and pressure, whether this is due to cycle design or operating mode. This is most universally applicable to ϵ_{SO_3} , but there is significant variability in the results.

Part of the variability can be explained by differences in Da, as given by Eq.(3). Oxidation ratios are plotted against Da in Figure 4. Approximate geometries and gas path velocities define the flow residence time, and the chemical time-scale is based on Eq.(2) specified for conditions at the turbine inlet.

For SO_2 oxidation to SO_3 , increasing Da nonlinearly increases conversion efficiency. It should not be expected that a single scale can explain all variability, but the goodness of fit displayed ($R^2 > 0.98$) suggests that for SO_3 , overall cycle design and operating point are factors most important to distinguishing technological differences in ϵ_{SO_3} . The variability among engine types in intra-engine temperature and pressure as a function of time, as well as the influence of other trace chemical activity (with the exception of HO_x) are less influential.

In contrast, the correlation with Da is weaker for NO_y species, suggesting that such details have a more significant impact in determining technological trends for HONO and NO_2 . Outliers are highlighted in Figure 4. For NO_2 in particular, the kinetic rates can get faster or slower with progress through the gas path, and are sensitive to the temperature and pressure variation as a function of time, which leads to the more varied behavior for the different modes. In reference to Figure 2, this means that

the gradient of formation potential contours can either be in the direction of changes in temperatures and pressures along the gas path, or against them, depending on mode and cycle. This is a significant source of variance in the trends shown in Figure 3.

Sensitivity analyses presented in the next section further suggest EINO_x influences ϵ_{NO_2} and ϵ_{HONO} to a significant degree, and this is an additional source of variability in the results. In contrast, ϵ_{SO_3} , ϵ_{NO_2} , and ϵ_{HONO} are all minimally impacted by EIS over the parameter space examined, which indicates independence from fuel sulfur content (FSC). However, absolute emissions of SO_3 are not independent and vary proportionally with FSC. For SO_3 and HONO, the greatest conversion in the bulk flow is localized to the latter part of the HPT and early part of the LPT, earlier for SO_3 and later for HONO. Formation rates for NO_2 are almost constant with location through the post-combustion flow path. Because formation for NO_y species occurs in the LPT, scaling based on turbine inlet parameters as in Figure 4 is less useful.

Overall, ϵ_{SO_3} sourced to trace chemistry through the turbine and exhaust nozzle is typically 0.5-1% at higher power operating conditions, falling to values $< 0.1\%$ at low power modes. Only at the lowest temperature, lowest pressure over all cycles examined (typical of idle power for an older, in-service engine) is conversion of SO_3 to H_2SO_4 a significant fraction of SO_x oxidation. Trends for conversion to NO_y are more dependent on

Table 4. Specifications for rate parameter and initial condition uncertainty.

Rate parameters	
Reaction	$\Delta \log_{10}(k)$
$\text{H} + \text{O}_2 = \text{O} + \text{OH}$	0.3
$\text{HO}_2 + \text{OH} = \text{H}_2\text{O} + \text{O}_2$	0.3
$\text{H}_2\text{O} + \text{O} = 2\text{OH}$	0.2
$\text{SO}_2 + \text{O} (+\text{M}) = \text{SO}_3 (+\text{M})$	0.4
$\text{SO}_3 + \text{H}_2\text{O} = \text{H}_2\text{SO}_4$	0.5
$\text{SO}_3 + \text{O} = \text{SO}_2 + \text{O}_2$	0.4
$\text{SO}_2 + \text{OH} = \text{SO}_3 + \text{H}$	0.4
$\text{SO}_2 + \text{OH} (+\text{M}) = \text{HOSO}_2 (+\text{M})$	0.4
$\text{HOSO}_2 + \text{O}_2 = \text{SO}_3 + \text{HO}_2$	0.5
$\text{NO} + \text{O} (+\text{M}) = \text{NO}_2 (+\text{M})$	0.5
$\text{NO}_2 + \text{O} = \text{NO} + \text{O}_2$	0.1
$\text{NO}_2 + \text{H} = \text{NO} + \text{OH}$	0.1
$\text{NO} + \text{HO}_2 = \text{NO}_2 + \text{OH}$	0.4
$\text{HONO} + \text{OH} = \text{NO}_2 + \text{H}_2\text{O}$	0.3
$\text{NO} + \text{OH} (+\text{M}) = \text{HONO} (+\text{M})$	0.3
$\text{HONO} + \text{O} = \text{OH} + \text{NO}_2$	1.0

Initial conditions	
Species	$1 \sigma \text{EI}$ (unless noted otherwise)
CO_2	0.4%
H_2O	2.5%
O_2	1.0%
NO_x	15%
CO	21%
SO_x	35%
OH	$\text{OH} / 3$ to 3OH

Table 5. Sensitivity coefficients and marginal trends.

Values of $|S|$ smaller than 0.045 are considered insensitive to the perturbations and are not shown. For correlation coefficients (R^2) smaller than 0.2, $\Delta S(T)$ and $\Delta S(\tau)$ are randomly scattered and not shown.

Species	perturb O ₂			perturb CO		
	S	$\Delta S(T)$	$\Delta S(\tau)$	S	$\Delta S(T)$	$\Delta S(\tau)$
NO ₂				0.214		
HONO	-0.057	0.137	0.060	-0.065		0.264
HNO ₃	-0.039	0.273	0.157	0.095		
SO ₃	0.125	0.205	0.127			
H ₂ SO ₄	-0.005	0.273	0.189			
Species	perturb CO ₂			perturb H ₂ O		
	S	S	S	S	$\Delta S(T)$	$\Delta S(\tau)$
NO ₂						
HONO				0.060	0.205	
HNO ₃				0.088	0.205	0.157
SO ₃				-0.094		-0.106
H ₂ SO ₄	-0.045	-0.055	-0.050	0.922		-0.133
Species	perturb NO _y			perturb SO _x		
	S	$\Delta S(T)$	$\Delta S(\tau)$	S	$\Delta S(T)$	$\Delta S(\tau)$
NO ₂	0.805	-0.273	-0.294			
HONO	0.942					
HNO ₃	0.710	-0.752				
SO ₃	-0.036			0.999		
H ₂ SO ₄	-0.028			0.998		0.013
Species	perturb OH					
	S	$\Delta S(T)$	$\Delta S(\tau)$			
NO ₂	0.043	-0.137				
HONO	0.231		-0.504			
HNO ₃	0.373	-0.956	-0.830			
SO ₃	0.063		-0.080			
H ₂ SO ₄	0.061					

Trend	↑T		↑τ	
	SO _x	NO _y	SO _x	NO _y
O ₂	S↑	S↑	S↔	S↑
CO	S↔	S↔	S↑	S↓
CO ₂	S↓	S↓	S↔	S↑
H ₂ O	S↔	S↓	S↑	S↑
OH	S↔	S↓	S↔	S↓

cycle design, as results exhibit both increasing and decreasing ϵ_{NO_2} and ϵ_{HONO} as a function of operating mode. This is a result of the sensitivity of the NO_y kinetics to changes in temperature and pressure discussed previously in this section and is most evident for large engines. A good example in Figure 3 is where the largest thrust class simulated (highlighted in green) exhibits

a monotonic increase in ϵ_{NO_2} with decreasing operating mode. Apart from these exceptions, oxidation to HONO is typically 2% of NO_y at high power, falling to values similar to SO₃ at idle and approach, ~0.1%. Similarly, conversion to NO₂ in the turbine is typically 2.5% for higher power modes and <0.1% at low power. Note NO_y trends with power condition are generally opposite in the combustor. Calculated HNO₃ is produced at less than 0.3% NO_y for all cases.

6. UNCERTAINTY AND BIAS

In this section, we estimate the magnitude of three important sources of uncertainty in modeling trace species emissions from gas turbine engines: uncertainty in chemical kinetic rate parameters, uncertainty in initial conditions, and modeling uncertainty associated with the fidelity with which turbomachinery fluid mechanics are represented. Uncertainties in rate parameters and initial conditions, fundamental to all attempts to estimate intra-engine conversion efficiency, are addressed first in Section 6.1 using the calculations summarized in Section 5 as a basis. Sensitivities to initial conditions outlined in Section 6.1 will clarify the importance of combustor processing to subsequent oxidation through the turbine and exhaust nozzle. Section 6.2 then addresses the influence of turbomachinery fluid mechanics on conversion efficiency. From these results, we can infer the potential role of flow temperature and velocity non-uniformities in the combustor dilution zone. Figure 2 indicates the impact of these non-uniformities by the hatched area. On Figure 2, rate parameter and initial condition uncertainties would change the locations of iso- $\Delta\epsilon$ contours.

6.1. Rate parameters and initial conditions

Our analysis of sensitivity to rate parameter and initial condition uncertainties focuses on the 1-D treatment of the turbine flow presented in Section 5. Simulations were performed in which rate parameters and inlet species levels were individually perturbed for the 1-D analyses summarized in Figure 3 to determine changes in exit plane emission levels. First, as shown in Eq.(4) exit plane relative sensitivities S_β of a given species to a given model parameter, β , were computed by running the 1-D model with perturbation, $\delta\beta$. Then, relative sensitivities were multiplied by the estimated uncertainty, $\Delta\beta$, in the given parameter and summed in quadrature to yield the overall relative uncertainty ($\Delta X/X$) in the predicted species emission level as shown in Eq.(4).

$$S_\beta = \frac{1}{X_\beta} \left(\frac{\Delta X_\beta}{\delta\beta} \right) \quad (4)$$

$$\frac{\Delta X}{X} = \sqrt{\sum_\beta (S_\beta \cdot \Delta\beta)^2}$$

Uncertainties in rate parameters were obtained from literature reviews. Uncertainties in species initial conditions were specified as variances in EI (g/kg-fuel) by a relative standard deviation.

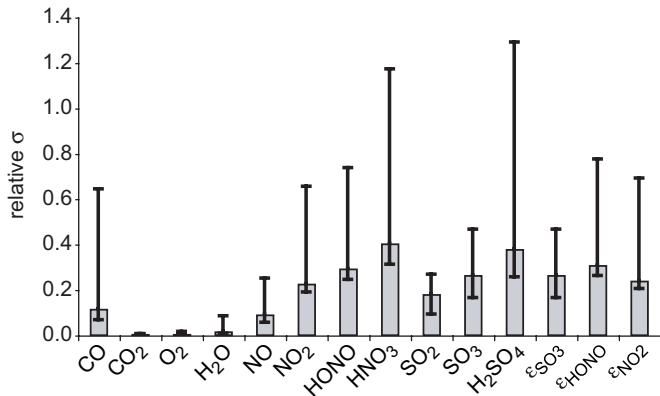


Figure 5. Relative uncertainties in species concentrations and conversion efficiencies.

These values represent the uncertainty in the original data used to specify emissions for the cycles simulated and are derived from variance in certification measurements and expected fuel composition. Specifications are summarized in Table 4.

Sensitivity to initial conditions is summarized in Table 5. In the table, S is the average sensitivity over all engine cycles and operating conditions, presented as the ratio of a percent change in an independent species at the turbine inlet (columns) referenced to the percent change in a dependent species at the engine exit (rows) on a molar basis. Results for S are highlighted in the blue columns. $\Delta S(T)$ and $\Delta S(\tau)$ are, respectively, the change in S from lowest to highest temperature cycle measured by T_4 (which correlates with oldest to newest technology, and low power to high power), and from the shortest residence time to longest. A negative trend is highlighted in red and a positive trend highlighted in green. Entries with insignificant values, here distinguished by an absolute value smaller than 0.045, are left blank.

Sensitivities are generally smaller than 1, and most of the sensitivity parameters that have significant values are correlated with turbine inlet temperature or residence time or both. Self-sensitivities are in the order of 1 and are dominant compared with other values, signifying the low level of direct interaction between SO_x and NO_y chemistry. Sensitivities of all species to O, H, and HO_2 are ~ 0 . Given the discussion in Section 4, the sensitivity to OH is expectedly larger, but still much less than 1, reinforcing the idea that SO_x and NO_y chemistries are a minor draw on the radical pool in comparison to reactions within the HO_x family, or among reactive oxidants generally. The correlation of sensitivity parameters with T_4 and residence time for all species and cycles can be summarized as shown at the bottom of Table 5. This is an alternate way of visualizing results for $\Delta S(T)$ and $\Delta S(\tau)$.

The analysis for rate parameters employed the full reaction mechanism listed in the Appendix, but we focus on major species inputs and dominant reactions identified using molar production rates and parametric sensitivity gradients. Figure 5 plots an estimate for the relative standard deviation for key species,

which sums contributions from variance in initial conditions and uncertainty in rate parameters. Similar estimates are also provided for ϵ_{SO_3} , ϵ_{NO_2} , and ϵ_{HONO} . The filled bars show the median values. The whiskers mark the minimum and maximum values to depict the potential range in relative uncertainty with changes in engine technology or operating condition.

The relative uncertainty in NO_y and SO_x species is seen to increase with oxidation state and is largest for the inorganic acids HNO_3 and H_2SO_4 . As a fraction of the total uncertainty, rate parameter variance is a small contribution relative to the impact of initial conditions for the major combustion products as well as NO and SO_2 . Rate parameter variance is roughly equal in importance to initial condition uncertainty for NO_2 and HONO. For SO_3 , H_2SO_4 , and HNO_3 , rate parameter uncertainties are dominant. To understand how these uncertainties impact ϵ for the turbine and exhaust nozzle, Figure 3 shows error bars around the median result in Figure 5 that represent uncertainty in ϵ . The magnitude of the variance due to rate parameter and initial condition uncertainty is less than the differences across engine types.

6.2. Temperature and velocity non-uniformities

Fluid mechanical phenomena have an important influence on oxidation in the SO_x family in the early stages of the turbine. In general, flow non-uniformities in the turbine flow can result in an increased opportunity for oxidation. To estimate the magnitude of impact, and thus the uncertainty in using a 1-D approximation, we demonstrate these influences using higher-fidelity computational tools to estimate the impact of fluid-chemical interactions through the first stage of a high pressure turbine typical of current, in-use engines. Turbomachinery reacting flows are computationally demanding. The scenarios presented were developed to capture the primary phenomena that affect trace chemistry for the high power operating conditions where ϵ_{SO_3} , ϵ_{NO_2} , and ϵ_{HONO} through the turbine and exhaust nozzle are highest. By inference, it should also be expected that temperature and velocity non-uniformities in the combustor should be similarly important for SO_x chemistry, but models addressing the relevant dilution jet and liner flows have not yet been developed.

The reacting flow solution for the multi-dimensional case was produced using the CNEWT code [1]. CNEWT combines well-established computational fluid dynamics and chemical kinetics solution mechanisms within a structure capable of calculating reacting internal flows. CNEWT is built on the NEWT turbomachinery CFD code [49], which employs a vertex-centered, finite-volume solution method incorporating a Runge-Kutta time discretization scheme to solve the full Reynolds-averaged Navier-Stokes, conservation of mass, and conservation of energy equations for three-dimensional geometries. Chemical mechanisms are represented using a system of ODEs handled through CHEMKIN routines and solved using VODE [50,51]. To complete the fluid-chemical integrations under the passive chemistry approximation in CNEWT, the flow and

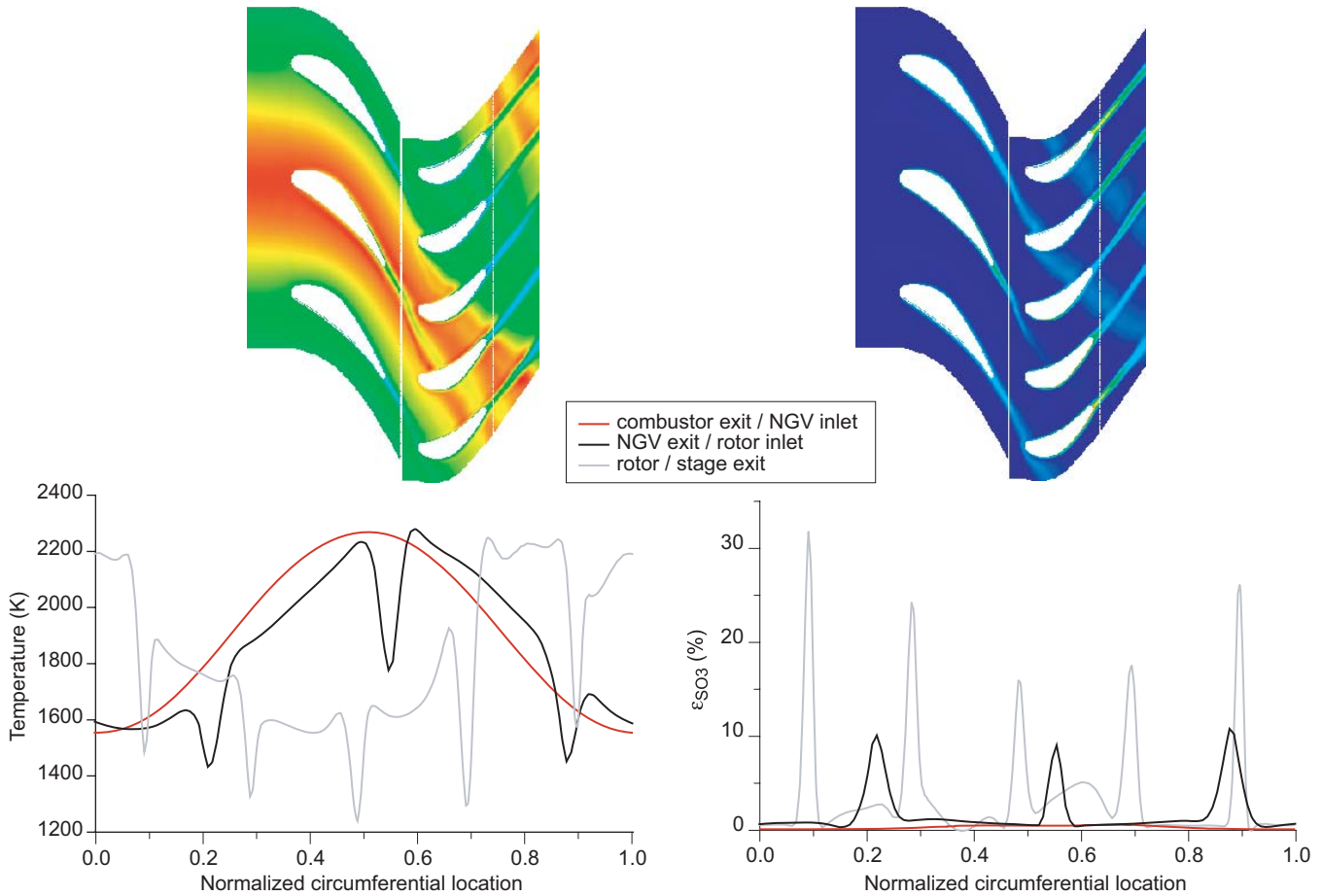


Figure 6. Distribution of SO_3 and temperature across a turbine stage.

chemistry algorithms are decoupled with the latter parallelized to better handle large systems of equations.

Computational grids were constructed so as to emphasize only circumferential and axial flows, thus establishing what is essentially a 2-D computation for the nozzle guide vane (NGV) and first HPT rotor. The radial dimension was ignored because the key fluid mechanics that impact chemistry are captured in the mid-span. This includes the impact of a cool boundary layer on oxidation, the impact of a non-uniform temperature profile at the combustor exit, the bulk evolution of species through the freestream, and the unsteady mixing of NGV blade wakes through the rotor. Three pitches for the NGV and five for the rotor were calculated simultaneously in separate calculations to match the periodicity of a typical engine turbine stage. These calculations were connected using an inlet mask to propagate the NGV flow into the rotor domain. Blade surfaces are set to a lower temperature boundary condition relevant to cooling air, but no film cooling mass is added in the solutions.

The variation in combustor exit properties represents the impact of typical exit non-uniformity, specified as a sinusoidal circumferential temperature profile with magnitude dependent on the given pattern factor. For a high efficiency, nearly

adiabatic combustor, changes in temperature at the combustor exit are related to the variation in the initial fuel-air ratio of the exhaust arriving at the exit. To calculate the fuel-air ratio profile, an adiabatic flame temperature calculation was performed to find the FAR associated with the temperature at each point on the combustor exit profile. The local FAR, temperature, and pressure thus constitute the necessary components for the initial condition specification conducted for each point specified for the temperature profile.

Figure 6 shows the distribution of SO_3 across the NGV and a snapshot across the rotor for the high power, high pattern factor, high sulfur case outlined in Table 2. Radial and circumferential temperature non-uniformities at the combustor exit plane act to segregate the chemically active regions of the turbine flow. This influence is evident with a 10-fold increase in oxidation to SO_3 as the highest temperature combustor flow moves over the cooled center blade, but smaller changes for the top and bottom blades (which are also cooled) where temperatures are lower. This difference occurs because of the increased residence time near the blade surface at temperatures favorable to SO_3 formation. For the equivalent low power case, the difference is more pronounced (although the enhancement is quantitatively

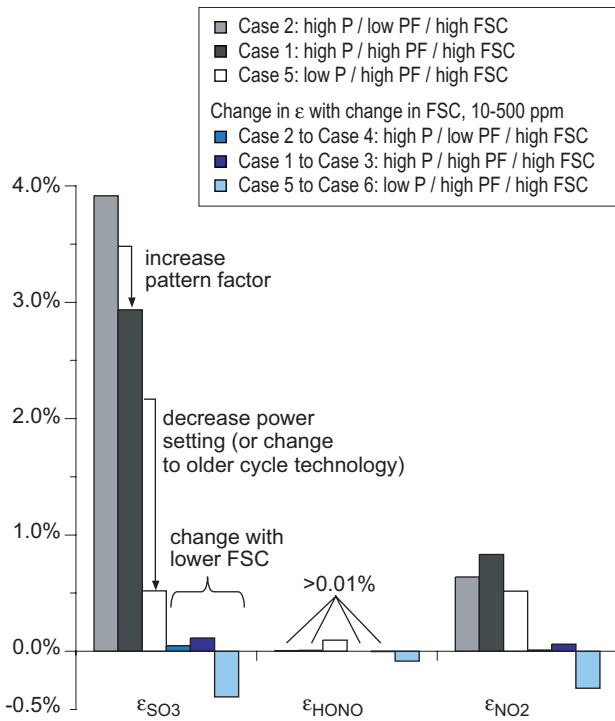


Figure 7. Effect of non-uniformity as a function of power setting (P), pattern factor (PF), and FSC.

smaller) and the increase happens only for sections exposed to the hotter flow.

Between blade rows, wake mixing occurs at constant pressure, and dilution of the oxidized sulfur with higher temperature air moves kinetics in the wake in the opposite direction from the near-blade effect. However, the mixing time-scale of wakes, which is generally on the order of the flow time through a full component or the full engine, is restricted by the row spacing. Thus, the boundary layer enhancement persists as a permanent augmentation. This can be seen in Figure 6. Similar features to the NGV exit are found at the stage exit, and it can be seen that additional flow has been exposed to the cooled blade as upstream wakes are chopped and migrate through the rotor passage. Unsteady chopping of wakes into downstream blade rows enhances mixing by increasing interfacial surface area, but this is a minor effect. The net impact is an increase in oxidation through the stage resulting from temperature gradients near the blade.

Comparatively, the bulk flow exhibits very little change through the stage, which is the result a 1-D analysis would suggest. This difference is illustrated notionally in Figure 2. The solid line represents the 1-D analysis, the evolution of mean temperature and pressure through the engine. The shaded area depicts the range of temperatures across the blade row. Only a small fraction of the flow move through these regions, but it can be seen that the cooler regions enable higher conversion efficiencies. The dashed line is included to suggest the persistence

of these temperature changes through the engine. Since trace chemical activity is slow compared to turbulent time-scales, the dominant role of turbulence should be in determining mixing rates, and we expect the k- ϵ model employed to approximately capture this effect. Increased turbulence will increase mixing, affecting temperature gradients in the flow, and decreasing the overall conversion efficiency.

Similar features are evident for both HONO and NO_2 , but since HONO production potential is significant only later in the gas path at the conditions simulated, temperature and residence time non-uniformities in this set of calculations have less impact on HONO as compared to NO_2 and SO_3 . This can be seen in Figure 7, which summarizes ensemble-averaged results from all multi-dimensional simulations outlined in Table 2. Sensitivities and uncertainties in rate parameters and initial conditions discussed in the previous section apply equally to these results. In particular, we would expect to find a similar influence from changing the $EINO_x$ as presented previously.

The lack of HONO response is generally applicable only to the extent that non-uniformities are less significant at locations downstream in the gas path where HONO is more active. For SO_3 , the impact of power setting is the most important factor, suggesting that non-uniformity effects predominate at higher power modes and for more recent engines. The influence of pattern factor depends on the response of oxidation rates to temperature variations, with a 1% increase in ϵ_{SO_3} and a 0.2% decrease in ϵ_{NO_2} resulting from a factor of 3 decrease in pattern factor. Except for the low power condition, variation in sulfur level has an insignificant impact based on our estimation of the absolute accuracy limits of the numerical calculation. At low power, altering the fuel sulfur level from 500 ppm to 10 ppm results in 0.4% reduction in ϵ_{SO_3} , which is comparable to the total oxidation through the stage at high FSC. However, in context, note that most conversion for the lower power conditions occurs within the combustor.

Secondary flows, mass injection through the blade, and endwall boundary layers were not modeled, but we can provide some evaluation of the direction of influence. Endwall cooling can enhance stage oxidation since the cooled surface area at the blade row hub and casing is comparable to cooled blade surface area. For mass injection, sensitivity results suggest that added O_2 would tend to increase production of SO_3 , but decrease HONO and NO_2 . However, cooling schemes are generally of high film effectiveness across the blade surface, and the resulting unmixedness may keep the freestream flow at a higher temperature than depicted in the solutions shown in Figure 6, reducing reactivity and thus oxidation [52]. Comparatively, this change in the temperature to which the SO_x chemistry would be exposed is stronger than the impact of compositional changes (O_2), suggesting that the augmentations in conversion shown would be lower with mass injection represented.

Based on a comparison between 1-D model approximations to the 2-D solutions, it is estimated that flow non-uniformities account for an additional 0-2% SO_x conversion to SO_3 for each

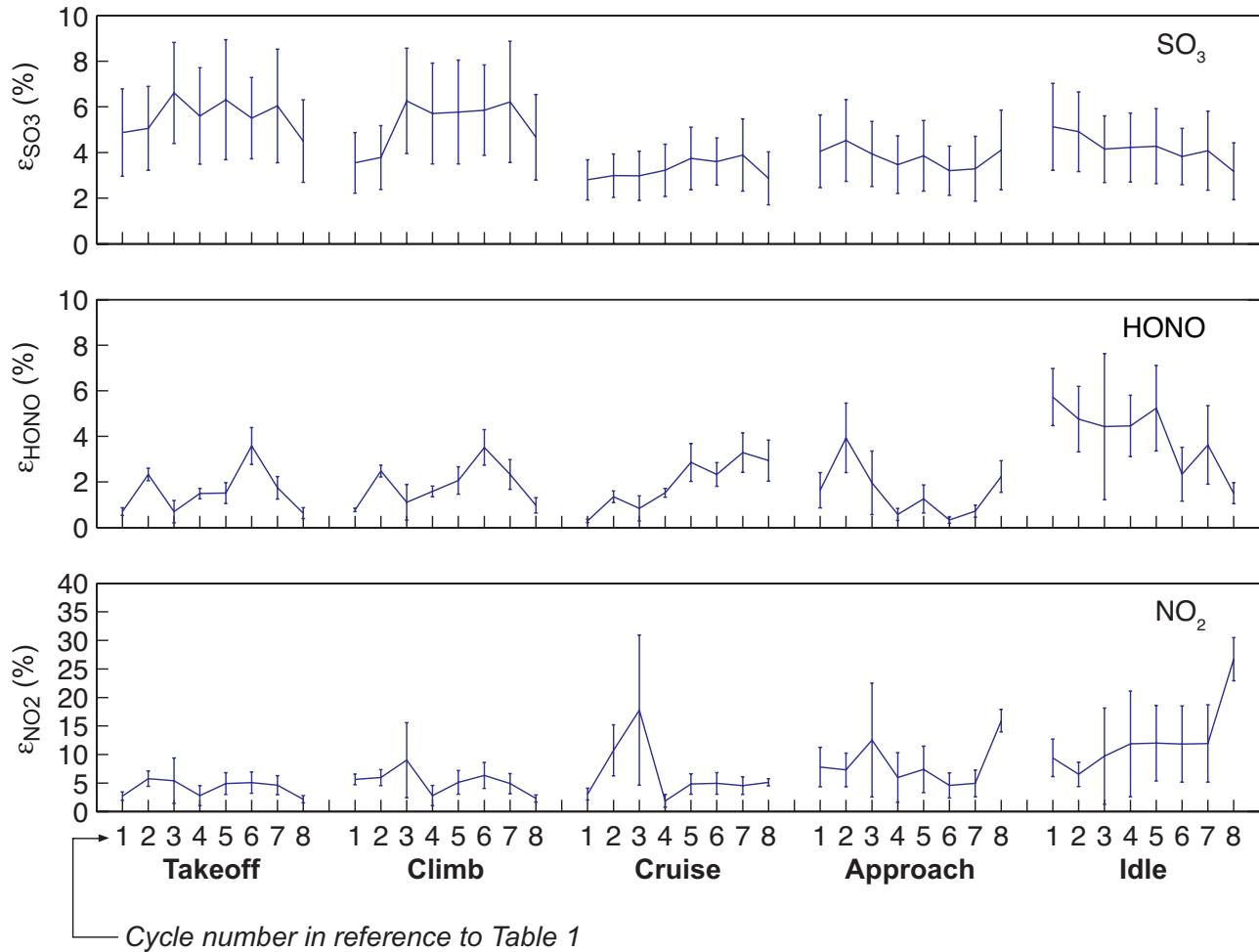


Figure 8. Best estimate conversion efficiencies (ϵ_{SO_3} , ϵ_{HONO} , and ϵ_{NO_2}) as a function of technology and operating mode.

cooled turbine stage. The higher end of this range is relevant to high power conditions or, equivalently, higher temperature cycles. This can be a significant fraction of the total conversion efficiency realized at the engine exit and thus represents a bias error in using 1-D analyses to predict exit emissions of sulfate aerosol precursors. In-service engines typically carry 1-2 cooled stages.

While the simulations show spatial impacts on NO_y chemistry through the turbine stage, a summary conclusion regarding HONO and NO_2 is not clear. There is generally no oxidation to HONO at high power conditions through the turbine stage, and a small negative influence from temperature and velocity non-uniformities at low power of 0% to -0.5% for the stage. This is despite similarly enhanced near-blade oxidative activity as in the case of SO_3 . Downstream temperature forcing in regions of the flow path where HONO is more active would be lower in the absence of cooling. In reference to the technology trends outlined above, this suggests a 1-D analysis captures the bulk of the HONO activity through the turbine and exhaust nozzle, and further emphasizes that for low power conditions or

older engines, likely conversion to HONO after the combustor would be minimal. The magnitude of impact from temperature and velocity non-uniformities on NO_2 is comparable to the stage conversion, but the sign of impact for NO_2 was ambiguous, being a positive for high power and negative for low power. Given the trends exhibited in the 1-D analysis, it should be recognized that the design of the turbine is a significant influence on the sign of the result and we can at most estimate here that non-uniformities represent added variability in the 1-D simulations of $\pm 1\%$.

7. SUMMARY

Aerosol precursors form through the combustor dilution zone, turbine, and exhaust nozzle of gas turbine engines. The intra-engine environment is more important to the production of condensable volatile PM in the area near an aircraft than emissions processing in the engine plume. However, due to an inefficient combination of thermodynamic and kinetic factors, there is overall little opportunity for the production of SO_3 , the most likely of the precursors to result in volatile PM.

Comparing combustor ϵ_{SO_3} to conversion magnitudes

through the post-combustor gas path suggests that SO_3 production in older technology engines would tend to be located in the combustor whereas for more recent cycle designs, the turbine and exhaust nozzle have a more prominent role. Since the combustor is likely the dominant source of precursors for most power conditions, further research should focus on a more detailed investigation of the combustor.

Best estimates for aerosol precursor production from in-service commercial engines are summarized in Figure 8. The figure shows the conversion efficiencies for each of the 8 cycles examined at each of the 5 operating modes simulated (Table 1). The values shown result from a Monte Carlo simulation sampling from distributions based on the results of this analysis. The distribution of combustor oxidation is specified uniform, bounded by the minimum and maximum estimated ϵ over the cooling schedules and residence times summarized in Figure 3. A random value chosen from this distribution is added to the ϵ estimated for the turbine and exhaust nozzle as shown in Figure 3. Finally, a uniformly random value is selected on the interval 0-2% for ϵ_{SO_3} and added for cases similar to the high power conditions simulated to account for the impact of temperature and velocity non-uniformities. Similarly, a random value from the interval -0.5% to 0% for ϵ_{HONO} is added for low power cases, and a random value between -1% to 1% is added to all cases for ϵ_{NO_2} . The conversion efficiency estimated in this fashion is then perturbed to account for uncertainties related to uncertainty in rate parameters and initial conditions using the relevant value from Figure 5.

The mean results are consistent with measurements of sulfur and nitrogen precursors. Although HONO and NO_2 oxidation can be on the order of 10%, particularly at low power conditions, we would not expect nitrate contributions to particulate mass until well after the plume mixes with the atmosphere. Thus, the focus rests upon the conversion efficiency ϵ_{SO_3} to evaluate volatile PM emissions that may impact the surroundings near an aircraft. In contrast to NO_y species, SO_x chemistry is active over the entire operational range of aircraft currently in the fleet. The trends examined here suggest that mean ϵ_{SO_3} is limited to the range 2.8% to 6.5%. This reflects technological differences within the fleet, the variation in oxidative activity with operating mode, and modeling uncertainty. Note an additional 1-2% conversion to SO_3 , and up to 1% for HONO (and NO_y) may be realized in the plume.

Since fuel flow increases with power setting, the SO_3 , NO_2 , and HONO emissions rates (*e.g.* kg/s) will be higher at take-off and climb than that suggested by the conversion efficiencies in Figure 8. Subsequently, for the landing take-off cycle, higher levels of sulfate in the near-field plume can be expected along the departure portion of a flight profile as opposed to landing. Assuming sulfur-derived volatile PM is most likely, these results suggest emission indices of 0.06-0.13 g/kg-fuel sourced to intra-engine conversion, assuming particles nucleated as $2\text{H}_2\text{SO}_4 \cdot \text{H}_2\text{O}$ for an FSC of 500 ppm (EIS of 0.5 g/kg-fuel). These values are similar to EIs for non-volatile particulate as interpreted from

measurements. Thus, on a mass basis, the impact of aviation volatile PM on local air quality is likely to be roughly comparable to the impact of aviation soot.

ACKNOWLEDGMENTS

This work is the product of several years of NASA support and more recently funding through the University of Missouri-Rolla Center of Excellence for Aerospace Propulsion Particulate Emissions Reduction. Many thanks go to Drs. Chowen Wey, Nan-Suey Liu, and Thomas Wey of the NASA Glenn Research Center for their thoughtful interactions with our group. The foundations of this work were established through the tireless efforts of current and former graduate students at MIT. Many thanks go to Tony Chobot, Pierre Dakhel, Sookhyun Han, and Chi Kin (Benny) Yam for their contributions to the understanding of aviation particulate matter emissions. Thank you also to Dave Dassault of Aerodyne and Jun Luo of Delta Search Labs for their assistance in assembling the literature review and uncertainty analysis presented in this paper.

REFERENCES

- [1] Lukachko, S.P., I.A. Waitz, R.C. Miake-Lye, R.C. Brown, and M.R. Anderson, 1998, "Production of sulfate aerosol precursors in the turbine and exhaust nozzle of an aircraft engine," *Journal of Geophysical Research-Atmospheres*, 103(D13), pp. 16159-16174.
- [2] U.S. Environmental Protection Agency, EPA, 2004, "Air quality criteria for particulate matter, Volumes 1 and 2," EPA/600/P-99/002bF, National Center for Environmental Assessment-RTP Office, Office of Research and Development, Research Triangle Park, N.C.
- [3] Intergovernmental Panel on Climate Change, 1999, "Aviation and the global atmosphere: A special report of the Intergovernmental Panel on Climate Change," J.E. Penner, D.H. Lister, D.J. Griggs, D.J. Dokken, and M. McFarland, eds., Cambridge University Press, Cambridge, UK.
- [4] Schumann, U., H. Schlager, F. Arnold, J. Ovarlez, H. Kelder, Ø. Hov, G. Hayman, I.S.A. Isaksen, J. Staehelin, and P.D. Whitefield, 2000, "Pollution from aircraft emissions in the North Atlantic flight corridor: Overview on the POLINAT projects," *Journal of Geophysical Research-Atmospheres*, 105(D3), pp. 3605-3631.
- [5] Anderson, B.E., W.R. Cofer, D.R. Bagwell, J.W. Barrick, C.H. Hudgins, and K.E. Brunke, 1998, "Airborne observations of aircraft aerosol emissions I: Total nonvolatile particle emission indices," *Geophysical Research Letters*, 25(10), pp. 1689-1692.
- [6] Miake-Lye, R.C., B.E. Anderson, W.R. Cofer, H.A. Wallio, G.D. Nowicki, J.O. Ballenthin, D.E. Hunton, W.B. Knighton, T.M. Miller, J.V. Seeley, and A.A. Viggiano, 1998, "SO_x oxidation and volatile aerosol in aircraft exhaust plumes depend on fuel sulfur content," *Geophysical Research Letters*, 25(10), pp. 1677-1680.

- [7] Anderson, B.E., W.R. Cofer, J.D. Barrick, D.R. Bagwell, and C.H. Hudgins, 1998, "Airborne observations of aircraft aerosol emissions II: Factors controlling volatile particle production," *Geophysical Research Letters*, 25(10), pp. 1693-1696.
- [8] Döpelheuer, A., 2001, "Quantities, characteristics and reduction potentials of aircraft engine emissions," SAE 2001-01-3008, *World Aviation Congress & Exposition*, Society of Automotive Engineers, Seattle, WA.
- [9] Karcher, B., 1997, "Heterogeneous chemistry in aircraft wakes: Constraints for uptake coefficients," *Journal of Geophysical Research-Atmospheres*, 102(D15), pp. 19119-19135.
- [10] Yu, F.Q., R.P. Turco, and B. Karcher, 1999, "The possible role of organics in the formation and evolution of ultra-fine aircraft particles," *Journal of Geophysical Research-Atmospheres*, 104(D4), pp. 4079-4087.
- [11] Schumann, U., F. Arnold, R. Busen, J. Curtius, B. Karcher, A. Kiendler, A. Petzold, H. Schlager, F. Schroder, and K.H. Wohlfrom, 2002, "Influence of fuel sulfur on the composition of aircraft exhaust plumes: The experiments SULFUR 1-7," *Journal of Geophysical Research-Atmospheres*, 107(D15).
- [12] Brown, R.C., M.R. Anderson, R.C. MiakeLye, C.E. Kolb, A.A. Sorokin, and Y.Y. Buriko, 1996, "Aircraft exhaust sulfur emissions," *Geophysical Research Letters*, 23(24), pp. 3603-3606.
- [13] Tremmel, H.G. and U. Schumann, 1999, "Model simulations of fuel sulfur conversion efficiencies in an aircraft engine: Dependence on reaction rate constants and initial species mixing ratios," *Aerospace Science and Technology*, 3(7), pp. 417-430.
- [14] Starik, A.M., A.M. Savel'ev, N.S. Titova, and U. Schumann, 2002, "Modeling of sulfur gases and chemions in aircraft engines," *Aerospace Science and Technology*, 6(1), pp. 63-81.
- [15] Reiner, T. and F. Arnold, 1993, "Laboratory Flow Reactor Measurements of the Reaction $\text{SO}_3 + \text{H}_2\text{O} + \text{M} \rightarrow \text{H}_2\text{SO}_4 + \text{M}$, Implications for Gaseous H_2SO_4 and Aerosol Formation in the Plumes of Jet Aircraft," *Geophysical Research Letters*, 20(23), pp. 2659-2662.
- [16] Karcher, B., R. Busen, A. Petzold, F.P. Schroder, U. Schumann, and E.J. Jensen, 1998, "Physicochemistry of aircraft-generated liquid aerosols, soot, and ice particles - 2. Comparison with observations and sensitivity studies," *Journal of Geophysical Research-Atmospheres*, 103(D14), pp. 17129-17147.
- [17] Schröder, F.P., B. Karcher, A. Petzold, R. Baumann, R. Busen, C. Hoell, and U. Schumann, 1998, "Ultrafine aerosol particles in aircraft plumes: *In situ* observations," *Geophysical Research Letters*, 25(15), pp. 2789-2792.
- [18] Schumann, U., J. Strom, R. Busen, R. Baumann, K. Gierens, M. Krautstrunk, F.P. Schroder, and J. Stingl, 1996, "*In situ* observations of particles in jet aircraft exhausts and contrails for different sulfur-containing fuels," *Journal of Geophysical Research-Atmospheres*, 101(D3), pp. 6853-6869.
- [19] Kolb, C.E., J.T. Jayne, D.R. Worsnop, M.J. Molina, R.F. Meads, and A.A. Viggiano, 1994, "Gas phase reaction of sulfur trioxide with water vapor," *Journal of the American Chemical Society*, 116(22), pp. 10314-10315.
- [20] Karcher, B., T. Peter, and R. Ottmann, 1995, "Contrail Formation - Homogeneous Nucleation of $\text{H}_2\text{SO}_4/\text{H}_2\text{O}$ Droplets," *Geophysical Research Letters*, 22(12), pp. 1501-1504.
- [21] Yu, F.Q. and R.P. Turco, 1997, "The role of ions in the formation and evolution of particles in aircraft plumes," *Geophysical Research Letters*, 24(15), pp. 1927-1930.
- [22] Brown, R.C., R.C. MiakeLye, M.R. Anderson, C.E. Kolb, and T.J. Resch, 1996, "Aerosol dynamics in near-field aircraft plumes," *Journal of Geophysical Research-Atmospheres*, 101(D17), pp. 22939-22953.
- [23] Karcher, B., 1998, "Physicochemistry of aircraft-generated liquid aerosols, soot, and ice particles - 1. Model description," *Journal of Geophysical Research-Atmospheres*, 103(D14), pp. 17111-17128.
- [24] Karcher, B., 1999, "Aviation-produced aerosols and contrails," *Surveys in Geophysics*, 20(2), pp. 113-167.
- [25] Dakhel, P.M., S.P. Lukachko, I.A. Waitz, R.C. Brown, and R.C. Miake-Lye, 2005, "Post-combustion evolution of soot properties in an aircraft engine," *GT2005-69113, ASME Turbo Expo 2005*, American Society of Mechanical Engineers, Reno-Tahoe, Nevada.
- [26] Miake-Lye, R.C., R.C. Brown, M.R. Anderson, and C.E. Kolb, 1994, "Calculations of condensation and chemistry in an aircraft contrail," *Impact of Emissions from Aircraft and Spacecraft Upon the Atmosphere*, Koln, Germany
- [27] Gleitsmann, G. and R. Zellner, 1999, "The aerosol dynamics of $\text{H}_2\text{O}-\text{H}_2\text{SO}_4-\text{HNO}_3$ mixtures in aircraft wakes. A modeling study," *Physical Chemistry Chemical Physics*, 1(24), pp. 5503-5509.
- [28] Detwiler, A.G. and A. Jackson, 2002, "Contrail formation and propulsion efficiency," *Journal of Aircraft*, 39(4), pp. 638-644.
- [29] Travis, D.J., A.M. Carleton, and R.G. Lauritsen, 2002, "Climatology: Contrails reduce daily temperature range, A brief interval when the skies were clear of jets unmasked an effect on climate," *Nature*, 418(6898), pp. 601-601.
- [30] Boucher, O., 1999, "Air traffic may increase cirrus cloudiness," *Nature*, 397(6714), pp. 30-31.
- [31] Meyer, R., H. Mannstein, R. Meerkotter, U. Schumann, and P. Wendling, 2002, "Regional radiative forcing by line-shaped contrails derived from satellite data," *Journal of Geophysical Research-Atmospheres*, 107(D10).
- [32] Marquart, S., M. Ponater, F. Mager, and R. Sausen, 2003, "Future development of contrail cover, optical depth, and radiative forcing: Impacts of increasing air traffic and climate change," *Journal of Climate*, 16(17), pp. 2890-2904.
- [33] Minnis, P., J.K. Ayers, R. Palikonda, and D. Phan, 2004, "Contrails, cirrus trends, and climate," *Journal of Climate*, 17(8), pp. 1671-1685.

- [34] Schumann, U., 2003, Aviation, Atmosphere, and Climate—What has been learned, *European Conference on Aviation, Atmosphere and Climate (AAC), Proceedings of an International Conference*, European Commission, Friedrichshafen, Germany, pp. 349-351.
- [35] Arnold, F., T. Stilp, R. Busen, and U. Schumann, 1998, “Jet engine exhaust chemiion measurements: Implications for gaseous SO₃ and H₂SO₄,” *Atmospheric Environment*, 32(18), pp. 3073-3077.
- [36] Curtius, J., F. Arnold, and P. Schulte, 2002, “Sulfuric acid measurements in the exhaust plume of a jet aircraft in flight: Implications for the sulfuric acid formation efficiency,” *Geophysical Research Letters*, 29(7).
- [37] Katragkou, E., S. Wilhelm, F. Arnold, and C. Wilson, 2004, “First gaseous sulfur (VI) measurements in the simulated internal flow of an aircraft gas turbine engine during project PartEmis,” *Geophysical Research Letters*, 31(2).
- [38] Karcher, B., R.P. Turco, F. Yu, M.Y. Danilin, D.K. Weisenstein, R.C. Miake-Lye, and R. Busen, 2000, “A unified model for ultrafine aircraft particle emissions,” *Journal of Geophysical Research-Atmospheres*, 105(D24), pp. 29379-29386.
- [39] Harris, B.W., 1990, “Conversion of sulfur dioxide to sulfur trioxide in gas turbine exhaust,” *Journal of Engineering for Gas Turbines and Power-Transactions of the ASME*, 112(4), pp. 585-589.
- [40] Arnold, F., J. Scheid, T. Stilp, H. Schlager, and M.E. Reinhardt, 1992, “Measurements of jet aircraft emissions at cruise altitude-I, the odd nitrogen gases NO, NO₂, HNO₂ and HNO₃,” *Geophysical Research Letters*, 19(24), pp. 2421-2424.
- [41] Whitefield, P., D.E. Hagen, K. Brundish, A.R. Clague, C.W. Wilson, R.C. Miake-Lye, R.C. Brown, J. Wormhoudt, S.P. Lukachko, A.T. Chobot, C.K. Yam, and I.A. Waitz, 2002, “NASA/QinetiQ Collaborative Program, Final Report,” NASA CR-2002-211900, NASA Glenn Research Center, U.S. National Aeronautics and Space Administration, Cleveland, Ohio.
- [42] Haschberger, P. and E. Lindermeir, 1997, “Observation of NO and NO₂ in the young plume of an aircraft jet engine,” *Geophysical Research Letters*, 24(9), pp. 1083-1086.
- [43] Miake-Lye, R.C., M. Martinez-Sanchez, R.C. Brown, and C.E. Kolb, 1993, “Plume and wake dynamics, mixing, and chemistry behind a high-speed civil transport aircraft,” *Journal of Aircraft*, 30(4), pp. 467-479.
- [44] Hunter, S.C., 1982, “Formation of SO₃ in gas turbines,” *Journal of Engineering for Power-Transactions of the ASME*, 104(1), pp. 44-51.
- [45] Wilson, C.W., A.R. Clague, M. Pourkashanian, and L. Ma, 2004, “Chemical kinetic modeling of the evolution of gaseous aerosol precursors within a gas turbine engine,” GT2004-53704, *ASME Turbo Expo 2004*, American Society of Mechanical Engineers, Vienna, Austria.
- [46] Mueller, M.A., R.A. Yetter, and F.L. Dryer, 2000, “Kinetic modeling of the CO/H₂O/O₂/NO/SO₂ system: Implications for high pressure fall-off in the SO₂+O(+M)=SO₃(+M) reaction,” *International Journal of Chemical Kinetics*, 32(6), pp. 317-339.
- [47] Glarborg, P., D. Kubel, K. DamJohansen, H.M. Chiang, and J.W. Bozzelli, 1996, “Impact of SO₂ and NO on CO oxidation under post-flame conditions,” *International Journal of Chemical Kinetics*, 28(10), pp. 773-790.
- [48] Brown, R.C., R.C. Miake-Lye, S.P. Lukachko, and I.A. Waitz, 2002, “Heterogeneous reactions in aircraft gas turbine engines,” *Geophysical Research Letters*, 29(10).
- [49] Dawes, W.N., 1992, “The simulation of 3-dimensional viscous flow in turbomachinery geometries using a solution-adaptive unstructured mesh methodology,” *Journal of Turbomachinery-Transactions of the ASME*, 114(3), pp. 528-537.
- [50] Brown, P.N., G.D. Byrne, and A.C. Hindmarsh, 1989, “VODE: a variable-coefficient ODE solver,” *SIAM Journal on Scientific and Statistical Computing*, 10(5), pp. 1038-1051.
- [51] Kee, R.J., F.M. Rupley, and J.A. Miller, 1991, “CHEMKIN-II: A FORTAN chemical kinetics package for the analysis of gas-phase chemical kinetics,” SAND89-8009, Sandia National Laboratories
- [52] Lukachko, S.P., D.R. Kirk, and I.A. Waitz, 2003, “Gas turbine engine durability impacts of high fuel-air ratio combustors, Part I: Potential for secondary combustion of partially reacted fuel,” *Journal of Engineering for Gas Turbines and Power*, 125(3), pp. 742-750.

APPENDIX

Reaction	A units: cm-mol-sec-K		
	E units = cal / mol		
troe = Troe form parameters low = low pressure form	A	b	E _a
1* H ₂ + M = H + H + M	4.57E+19	-1.4	104400
2 O + H ₂ = H + OH	5.08E+04	2.7	6290
3* O + O + M = O ₂ + M	6.16E+15	-0.5	0
4 H + O ₂ = O + OH	1.91E+14	0.0	16440
5* H + O ₂ (+M) = HO ₂ (+M)	1.48E+12	0.6	0
troe 0.5 / 1e-30 / 1e30 low→	3.482E+16	-0.411	-1115
6* H + O + M = OH + M	4.71E+18	-1.0	0
7 OH + H ₂ = H ₂ O + H	2.16E+08	1.5	3430
8 H ₂ O + O = OH + OH	2.97E+06	2.0	13400
9* H ₂ O ₂ (+M) = OH + OH (+M)	2.95E+14	0.0	48430
troe 0.5 / 1e-90 / 1e90 low→	0.12E+18	0.0	45500
10* OH + H + M = H ₂ O + M	2.21E+22	-2.0	0
11 HO ₂ + O = O ₂ + OH	3.25E+13	0.0	0
12 HO ₂ + H = H ₂ + O ₂	1.66E+13	0.0	823
13 HO ₂ + H = OH + OH	7.08E+13	0.0	295
14 HO ₂ + OH = H ₂ O + O ₂	2.89E+13	0.0	-497
15 HO ₂ + HO ₂ = H ₂ O ₂ + O ₂ (duplicate)	4.20E+14	0.0	11982
16 HO ₂ + HO ₂ = H ₂ O ₂ + O ₂ (duplicate)	1.30E+11	0.0	-1629
17 H ₂ O ₂ + O = OH + HO ₂	9.55E+06	2.0	3970
18 H ₂ O ₂ + H = H ₂ O + OH	2.41E+13	0.0	3970
19 H ₂ O ₂ + H = HO ₂ + H ₂	4.82E+13	0.0	7950
20 H ₂ O ₂ + OH = H ₂ O + HO ₂ (duplicate)	1.00E+12	0.0	0
21 H ₂ O ₂ + OH = H ₂ O + HO ₂ (duplicate)	5.80E+14	0.0	9557
22 HNO + H = NO + H ₂	4.40E+11	0.7	650
23† NO + O (+M) = NO ₂ (+M)	1.30E+15	-0.8	0
troe 0.957 / 1E-90 / 8.332E+03 low→	4.72E+24	-2.87	1551

Reaction	note	A units: cm-mol-sec-K		
		E units = cal / mol		
troe = Troe form parameters		A	b	E _a
low = low pressure form				
24 [†] NO + O (+M) = NO ₂ (+M)		1.52E+15	-0.4	0
troe 0.82 / 1E-90 / 1E+90	low→	3.1E+19	-1.32	735.2
25 [†] NO + OH (+M) = HONO (+M)		1.99E+12	-0.1	-721
troe 0.62 / 1E-90 / 1E+90	low→	5.08E+24	-2.51	-67.6
26 NO ₂ + H ₂ = HONO + H		7.33E+11	0.0	28810
27 NO ₂ + O = O ₂ + NO		1.05E+14	0.0	0.0
28 [†] NO ₂ + O (+M) = NO ₃ (+M)		1.33E+13	0.0	000
troe 0.826 / 1E-90 / 3.191E+03	low→	1.49E+29	-4.08	2467
29 NO ₂ + H = NO + OH		1.32E+14	0.0	362
30 [†] NO ₂ + OH (+M) = HNO ₃ (+M)		2.41E+13	0.0	0
troe 0.837 / 1E-90 / 1.657E+03	low→	6.42E+32	-5.49	2350
31 HO ₂ + NO = NO ₂ + OH		2.11E+12	0.0	-479
32 NO ₂ + NO ₂ = NO ₃ + NO		9.64E+09	0.7	20920
33 NO ₂ + NO ₂ = 2NO + O ₂		1.63E+12	0.0	26120
34 HNO + O = OH + NO		1.81E+13	0.0	0
35 HNO + OH = H ₂ O + NO		1.30E+07	1.9	-956
36 HNO + NO ₂ = HONO + NO		6.02E+11	0.0	1987
37 HONO + O = OH + NO ₂		1.20E+13	0.0	5961
38 HONO + OH = H ₂ O + NO ₂		1.70E+12	0.0	-520
39 HCO + M = H + CO + M		1.86E+17	-1.0	17000
40 [‡] HCO + O ₂ = CO + HO ₂		7.58E+12	0.0	410
41 HCO + O = CO + OH		3.02E+13	0.0	0
42 HCO + H = CO + H ₂		7.23E+13	0.0	0
43 HCO + OH = CO + H ₂ O		3.02E+13	0.0	0
44 [‡] CO + O (+M) = CO ₂ (+M)		1.80E+10	0.0	2384
troe: n/a	low→	1.35E+24	-2.788	4191
45 CO + O ₂ = CO ₂ + O		2.53E+12	0.0	47700
46 CO + OH = CO ₂ + H		1.40E+05	1.9	-1347
47 CO + HO ₂ = CO ₂ + OH		3.01E+13	0.0	23000
48 NO + HCO = HNO + CO		7.23E+12	0.0	0
49 NO ₂ + HCO = CO + HONO		1.26E+23	-3.3	2354
50 NO ₂ + HCO = H + CO ₂ + NO		8.43E+15	-0.8	1927
51 NO ₂ + CO = CO ₂ + NO		9.03E+13	0.0	33780
52 SO ₃ + O = SO ₂ + O ₂		4.40E+11	0.0	6100
53 SO ₃ + SO = SO ₂ + SO ₂		1.00E+12	0.0	4000
54 ^{**} SO ₂ + O (+M) = SO ₃ (+M)		9.20E+10	0.0	2384
troe: n/a	low→	4.00E+28	-4.0	5250
55 ^{††} SO ₂ + OH (+M) = HOSO ₂ (+M)		1.21E+12	0.0	0
troe 0.35 / 1E-30 / 1E+30	low→	1.87E+31	-4.61	2050
56 SO ₂ + OH = SO ₃ + H		4.90E+01	2.7	23800
57 ^{‡‡} SO + O (+M) = SO ₂ (+M)		3.20E+13	0.0	0
troe 0.55 / 1E-30 / 1E+30	low→	0.29E+25	-2.9	0
58 SO + OH = SO ₂ + H		5.20E+13	0.0	0
59 SO + OH + M = HOSO + M		8.00E+21	-2.2	830
60 SO + O ₂ = SO ₂ + O		6.20E+03	2.4	3050
61 HOSO + M = SO ₂ + H + M		5.90E+34	-5.7	50900
62 HOSO + OH = SO ₂ + H ₂ O		1.00E+12	0.0	0
63 HOSO + O ₂ = SO ₂ + HO ₂		1.00E+12	0.0	1000
64 HSO ₂ + M = SO ₂ + H + M		1.20E+28	-4.1	18900
65 HSO ₂ + M = HOSO + M		1.10E+21	-2.0	29900
66 HOSO ₂ = HOSO + O		5.40E+18	-2.3	106300
67 HOSO ₂ + M = SO ₃ + H + M		3.20E+16	-0.8	53700
68 HOSO ₂ + H = SO ₂ + H ₂ O		1.00E+12	0.0	0
69 HOSO ₂ + O = SO ₃ + OH		5.00E+12	0.0	0
70 HOSO ₂ + OH = SO ₃ + H ₂ O		1.00E+12	0.0	0
71 HOSO ₂ + O ₂ = SO ₃ + HO ₂		7.80E+11	0.0	656
72 SO ₂ + NO ₂ = SO ₃ + NO		6.30E+12	0.0	27000
73 SO ₃ + H ₂ O = H ₂ SO ₄		7.23E+08	0.0	0

Appendix notes:

- * Efficiencies for reactions 1, 3, 5, 6, 9, and 10:
H₂ = 2.5, H₂O = 12, CO = 1.9, CO₂ = 3.8, AR = 0.75
- † Efficiencies for reactions 23, 24, 25, 28, and 30: AR = 0.75
- ‡ Efficiencies for reactions 40 and 44 :
H₂ = 2.5, H₂O = 12, CO = 1.9, CO₂ = 3.8
- ** Efficiencies for reaction 54: N₂ = 1.3, H₂O = 12
- †† Efficiencies for reaction 55: H₂O = 10
- ‡‡ Efficiencies for reaction 57: N₂ = 1.5, H₂O = 10